Schweizerische Eidgenossenschaft
Confédération suisse
Confederazione Svizzera
Confederaziun svizra

Federal Department of the Environment, Transport, Energy and Communications DETEC

Swiss Federal Office of Energy SFOE
Energy Research and Cleantech Division

Final report dated 4th January 2022

Lowest-emission compression ignition combustion concepts using partial stratification and multiple injections (PCCI)

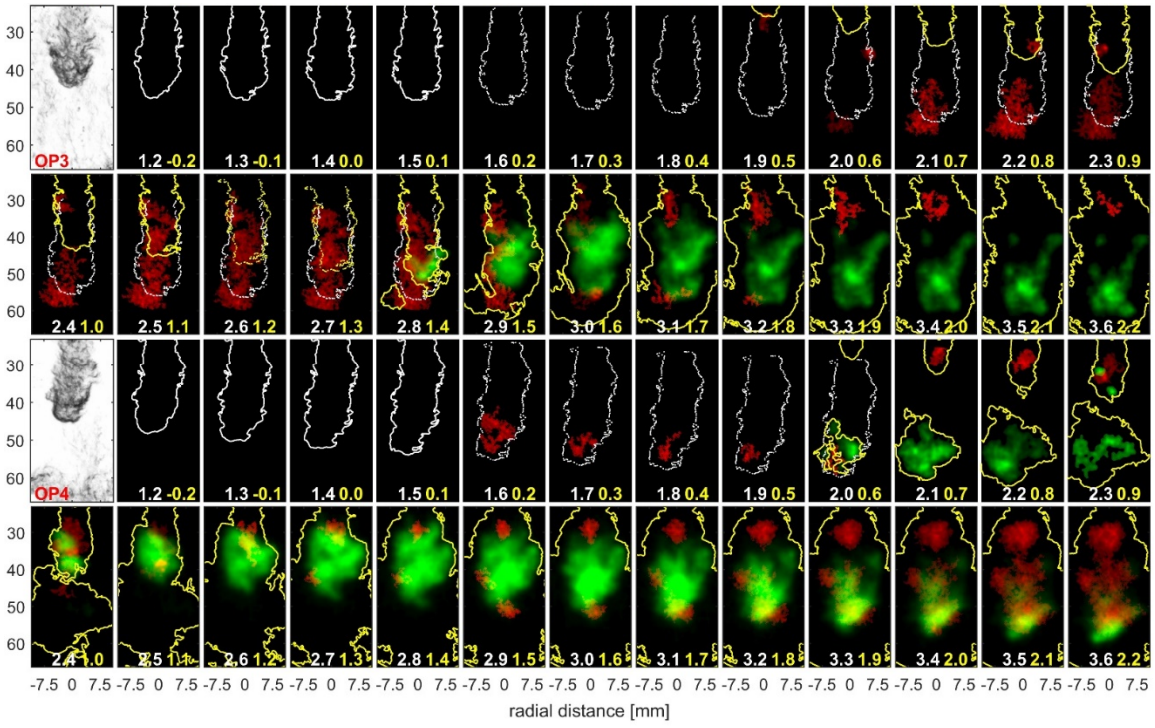

Source: ©Ulrich Doll, PSI 2020

Date: 4th January 2022

Location: Zurich

Publisher:
Swiss Federal Office of Energy SFOE
Energy Research and Cleantech
CH-3003 Bern
www.bfe.admin.ch

Co-financing:
CORNET/FVV Project "Premixed Diesel (PCCI)", IGF 244 EN, FVV 601352

Subsidy recipients:
ETH Zurich
Aerothermochemistry and Combustion Systems Laboratory
Institute of Energy and Process Engineering
ML J40, Sonneggstrasse 3
CH-8092 Zurich
www.lav.ethz.ch

Authors:
Dr. Ulrich Doll, PSI, ulrich.doll@psi.ch
Dr. Christos Altantzis, ETH Zurich, altantzis@lav.mavt.ethz.ch
MSc. Maria Martinez Garica, ETH Zurich, marmartinez@ethz.ch
Dr. Christophe Barro, ETH Zurich, barro@lav.mavt.ethz.ch
Dr. Yuri M. Wright, ETH Zurich, wright@lav.mavt.ethz.ch
Prof. Dr. Konstantinos Boulouchos ETH Zurich, boulouchos@lav.mavt.ethz.ch

SFOE project coordinators:
Dr. Carina Alles, Carina.Alles@bfe.admin.ch
Stephan Renz, info@renzconsulting.ch

SFOE contract number: SI/501744-01

The authors bear the entire responsibility for the content of this report and for the conclusions drawn therefrom.

Zusammenfassung

Mit dieselmotorischen Brennverfahren wird bei verschiedenen Lastzuständen ein sehr guter Wirkungsgrad bei gleichzeitig hohem Drehmoment erreicht. Dies sind Vorteile, die bei zahlreichen heavy-duty Anwendungen wie Langstreckentransport, Baumaschinen oder Schifffahrt eine zentrale Rolle spielen. Auch wenn fossile Dieseltreibstoffe in der Zukunft nicht mehr genutzt werden, sollen diese Brennverfahren verbessert werden für alternative Krafstoffe wie Biodiesel, Dimethyl-Ether (DME), Poly-oxymethylene-Dimethyl-Ether (OME) und langkettige synthetische Fischer-Tropsch Diesel. Vorgemischte Dieselverbrennungskonzepte (Premixed Charge Compression Ignition, PCCI) haben gegenüber typischen Dieselbrennverfahren erhebliches Potential, gleichzeitig NOx und Russemissionen zu reduzieren.

Aufgrund der leichten Stratifizierung in der Mischung durch mehrere gezielte Einspritzvorgänge werden Probleme mit der Steuerung des Brennbeginns, wie sie bei vollhomogenen Diesel Brennverfahren (Homogeneous Charge Compression Ignition, HCCI) auftreten, stark reduziert. Die experimentellen Untersuchungen wurden in einer optisch zugänglichen Schnellverdichtungs-Apparatur (Rapid Compression Expansion Machine, RCEM) durchgeführt mit unterschiedlichen Einspritzstrategien, welche Variationen der Last, Reaktivität und Stratifizierung repräsentieren. Nebst einer sorgfältigen thermodynamischen Analyse wurden optische Untersuchungen durchgeführt. Laser-Induzierte Fluoreszenz (LIF) Verfahren ermöglichten die quantitative Charakterisierung der zeitlichen Entwicklung des Mischungsfeldes sowie einer Spezies (Formaldehyd), welche den Zündvorgang abbildet. Die Hochtemperaturreaktionen wurden anhand von Schlieren- und OH* Chemilumineszenzaufnahmen ebenfalls raum- und zeitaufgelöst erfasst. Die Analyse der Mischungsfelder und Verbrennungsindikatoren haben neue Erkenntnisse über die Wechselwirkung von Mehrfacheinspritzungen hervorgebracht. Large Eddy Simulationen wurden zudem durchgeführt und zeigen gute Übereinstimmungen in Bezug auf die Brennraten sowie den Strukturen der Jets für die unterschiedlichen Betriebsbedingungen und ergänzten die experimentellen Untersuchungen bei der Interpretation der Wechselwirkungen und Zündprozesse von Mehrfacheinspritzungen. Die Simulation ermöglichte zudem Einblick in die Interaktion der ersten Einspritzung mit den Brennraumwänden, welche zu erheblicher Filmbildung führt und damit den relativ tiefen Brennstoffumsatz teilweise erklärt.

Das PCCI Konzept scheint deshalb besonders für Kraftstoffe mit niedrigerem Siedepunkt und hoher Zündwilligkeit ein attraktives Konzept zu sein. Insbesondere DME ist ein interessanter Kandidat. DME wird unter überkritischen Bedingungen eingespritzt, weist eine gute Gemischbildung auf, und eine signifikante Wandbeaufschlagung kann vermieden werden. Aufgrund des Fehlens von C-C-Bindungen wurde ausserdem bereits bei der herkömmlichen Diesel-Verbrennung eine geringe Verrussungsneigung nachgewiesen.

DME könnte deshalb ein idealer Brennstoff sein, um bei hoher Effizienz niedrigste Emissionen zu erreichen, indem verschiedene Verbrennungsmodi für bestimmte Motorlastpunkte eingesetzt werden. DME sollte daher in zukünftigen Studien weiter untersucht werden.

Summary

The conventional Diesel combustion concept enables very good efficiencies for a wide range of loads combined with high torque levels. These advantages are particularly important for a number of heavy-duty applications such as long-haul freight transport, off-road construction and agricultural machinery as well as shipping. Even though fossil fuels will be abandoned, the Diesel combustion process will continue to play an important role and hence requires improvements, especially with respect to alternative fuels such as Dimethyl-Ether (DME), Poly-oxymethylene-Dimethyl-Ether (OME) and long-chain synthetic Fischer-Tropsch fuels. Compared to conventional Diesel combustion concepts, Premixed Charge Compression Ignition (PCCI) has shown considerable potential to simultaneously reduce both particulate matter and NOx.

The tailored, slight mixture stratification stemming from multiple injections allows for more control of the combustion event compared to fully Homogenous Charge Compression Ignition Concepts (HCCI). The experimental investigations were carried out in a Rapid Compression Expansion Machine (RCEM) using different injection strategies, representing changes in load, reactivity and level of stratification. Aside dedicated thermodynamic analyses optical investigations were performed. Tracer Laser-Induced Fluorescence high-speed imaging allowed for quantification of the spatio-temporal evolution of the mixing field. The ignition process was characterized by means of formaldehyde LIF while high-speed Schlieren and OH* chemiluminescence provided information on the high-temperature combustion process. The analysis of the mixing fields and combustion indicators provided new insights with respect to the interactions between multiple injections. Large Eddy Simulations have further been performed, showing good agreement in terms of heat release rates and jet structure evolutions for the different operating conditions. The numerical results complemented the experimental findings in terms of interpretation of the interactions and ignition process. In addition, the simulation provided insights on the interaction of the first injection with the combustion chamber walls leading to significant film formation, explaining in part the relatively low overall fuel conversion rate.

PCCI can therefore be considered particularly attractive for low boiling point fuels with high ignition propensity. In particular DME, which is injected at supercritical conditions, thereby promoting mixture formation and avoiding significant spray-wall interaction is an interesting candidate. Due to the absence of C-C bonds, DME has shown very low sooting propensity even under conventional Diesel operation.

DME could therefore be an ideal candidate fuel to achieve highest efficiency with lowest emissions for a variety of combustion modes at specific operating conditions and should be further investigated in future studies.

Main findings

- Optical diagnostics, complemented by Large-Eddy Simulations with detailed kinetics of Premixed Charge Compression Ignition (PCCI) in a Rapid Compression Expansion Machine at engine conditions were carried out. Good agreement of the predictions with the experiments is reported for variations in operating conditions corresponding to changes in load, reactivity and stratification
- The combination of experimental and numerical methods at engine relevant conditions provides new insights into the evolutions of the mixing fields for multiple injections as well as the interplay between mixing and chemical reactions leading to ignition and partially premixed fuel conversion, thereby avoiding mixing-controlled regimes (and hence soot formation)
- The simulation provided additional insights to jet-wall interactions in the non-observable part of the experimental domain, suggesting considerable film formation and near-wall fuel concentration, thereby partially explaining the low overall fuel conversion observed thermodynamically
- Further work is needed to assess emission formation, develop improved injection strategies which avoid significant near-wall fuel concentrations, and, in particular to assess the potential of novel/synthetic fuels with favourable evaporation/mixing and combustion properties for PCCI

Contents

Zusammenfassung ... **3**

Summary ... **3**

Main findings ... **4**

Contents ... **5**

Abbreviations ... **7**

1 Introduction ... **8**

1.1 Background information and current situation ... 8

1.2 Purpose of the project ... 8

1.3 Objectives ... 9

2 Description of experimental facility ... **9**

2.1 Rapid compression and expansion machine ... 9

3 Procedures and methodology ... **10**

3.1 Operating strategy and heat release rate analysis ... 10

3.2 Optical diagnostics ... 12

3.2.1 Instrumentation ... 12

3.2.2 Data acquisition and evaluation of optical data ... 13

3.3 Computational Fluid Dynamics methodology ... 15

3.4 Resolution study ... 16

3.4.1 Free Spray Analysis ... 16

3.4.2 First Injection Analysis. RCEM geometry. ... 18

3.4.3 Computational cost ... 20

4 Results and discussion ... **21**

4.1 Jet metrics ... 21

4.2 Mixing dynamics ... 22

4.2.1 Local mixing phenomena ... 23

4.2.2 Global mixing state ... 24

4.3 Combustion analysis ... 27

4.3.1 Thermodynamic analysis and global combustion metrics ... 27

4.4 Ignition characteristics ... 29

4.5 Detailed analysis of simulated ignition processes ... 34

4.5.1 Effect of chemistry mechanism employed ... 36

4.5.2 Effect of film modelling ... 37

4.6 Exploratory numerical simulation of engine relevant conditions ... 38

5 Conclusions 40
6 Outlook and next steps 42
7 National and international cooperation 43
8 Publications 43
9 References 43

Abbreviations

AMR	Adaptive Mesh Refinement
BDC	Bottom Dead Centre
CFD	Computational Fluid Dynamics
CVC	Constant Volume Cell
EGR	Exhaust Gas Recirculation
HCCI	Homogeneous Charge Compression Ignition
HRR	Heat Release Rate
HT	High Temperature
LES	Large Eddy Simulation
LIF	Laser Induced Fluorescence
LT	Low Temperature
LTC	Low Temperature Combustion
ODE	Ordinary Differential Equation
OP	Operating Point
PCCI	Premixed Charge Compression Ignition
PDF	Probability Distribution Function
MFB	Mass Fraction Burned
SGS	Sub-Grid Scale
SOI	Start Of Injection
TDC	Top Dead Centre
UHC	Unburnt Hydro-Carbons

1 Introduction

1.1 Background information and current situation

The need both to reduce CO_2 emissions as well as to meet aggravated pollutant emission targets poses significant challenges to the mobility sector. In this context, low temperature combustion (LTC) concepts for direct-injection diesel engines are of great interest, since they have the potential to increase overall engine efficiency while at the same time reducing pollutant NOx and soot emissions [1]. In contrast to the mixing controlled combustion in conventional diesel engines (where the process limiting rate is dominated by mixing rather than reaction kinetics), promising LTC concepts such as Homogeneous Charge Compression Ignition (HCCI) employ extensive premixing to create a homogeneous lean fuel-air cylinder charge. This charge then simultaneously auto-ignites at multiple spots towards the end of the compression stroke, resulting in faster heat release and pressure rise at significantly lower peak temperatures [2]. Being beneficial in terms of emissions and efficiency, however, a potential drawback of the HCCI concept lies in the challenging control of the combustion process. Other than in fuel mixing controlled conventional diesel or spark-ignited gasoline combustion, the HCCI rate limiting process is reaction kinetics, which are influenced by a complex interplay of mixture preparation and temperature control of ignition timing through intake air heating, exhaust gas recirculation (EGR) or exhaust valve closing timing [1, 3-6]. In this context, hybrid combustion concepts such as Premixed Charge Compression Ignition (PCCI) offer a huge potential to combine high efficiency/low emission characteristics of HCCI with the superior operability of conventional diesel combustion [5]. In PCCI, the rate limiting processes from conventional diesel (mixing) and HCCI (reaction kinetics) are approaching similar levels. This can either be achieved by the choice of the fuel, which affects the reaction kinetics or by the choice of the injection strategy, which affects the mixing. The current work focuses on the injection strategy.

The PCCI combustion strategy involves fuel injection early in the compression stroke allowing for a certain degree of in-cylinder premixing in order to keep combustion temperatures low and, thereby, avoiding NOx and soot formation. In general, ignition control in PCCI is achieved through high EGR rates [7] or intake condition variations such as varying temperature, pressure or fuel reactivity by blending with low cetane fuels [5]. In addition to above control mechanisms influencing combustion chemistry and in contrast to the HCCI approach, PCCI implementations retain the coupling between start of injection and start of combustion [5, 8]. The latter is especially attractive since it offers the opportunity to use standard injection systems instead of specialized hardware. The current study aims at investigating the mixing and ignition fundamentals of PCCI combustion in applying multiple injections.

1.2 Purpose of the project

Fuel split by multiple injections is an established strategy to reduce pollutant emissions in diesel combustion while increasing fuel economy [9-12]. Additionally, multiple injections can be applied to tailor fuel-air mixing [13-15] and ignition timing [14, 15] as well as to reduce unburned hydrocarbons (UHC) and CO by preventing fuel wetting and flame quenching at the piston wall [14, 16, 17]. In [18] the reaction kinetics using various fuels under HCCI conditions were studied and modelled. The effect of mixing various injection durations was investigated in [19]. It was shown, that the role of low temperature combustion is increasingly important with shorter injection duration. In the PCCI concept, the role of detailed reaction kinetics separating low and high temperature combustion effects in combination with the mixing behavior of short injections, embedded in a split injection schedule are expected to be important. However, understanding of the complex interplay between the relevant operational parameters, fuel-air mixing and combustion chemistry affecting the PCCI combustion process is still scarce and optical diagnostics play a crucial role in providing detailed spatially and temporally resolved insights into the underlying mechanisms. Bruneaux and Maligne [20] carried out a detailed study of the mixing and combustion behavior of short double diesel injections in a constant volume cell (CVC). The

authors observed significantly enhanced mixing at the spray tip of the second injection caused by the flow field of the preceding injection. In addition, it was found that low-temperature combustion intermediates of the first injection were entrained by the subsequent jet, leading to an accelerated high-temperature ignition process. In [21], the study of double injections of n-dodecane by Schlieren imaging and planar laser induced fluorescence (PLIF) of formaldehyde within a CVC confirmed faster penetration and mixing rates of the second jet by entering a kind of “slipstream”, thus benefiting from the sustained momentum and turbulence of the previous injection. In support of the findings of [20, 22], the authors conclude that the ignition delay of the second jet is significantly reduced by the interaction with cold-flame reaction products of the first injection. At varying ambient temperatures from 900 K to 750 K, combustion efficiency was reduced from 95 % to 75 % and a persistent formaldehyde PLIF signal was associated with an incomplete high-temperature combustion process. By investigating the spray tip penetration of double injection schemes in an optical two-stroke engine using Schlieren diagnostics, Desantes et al. [23] confirmed the “slipstream” hypothesis and found a distinct relationship of faster penetration rates and shorter dwell times between injections as well as reduced ignition delays of the second compared to the preceding jet.

1.3 Objectives

Even though above works provided valuable insights into how multiple injections influence mixing and combustion processes, discussed results were predominantly obtained at constant ambient densities and, therefore, lack the transient behavior of a full engine cycle. In addition, the studies focus on the interaction between the consecutive injections or mixing behavior of single injections rather than providing necessary operational characteristics for PCCI strategies such as mixture preparation. In this context, the current study aims at providing detailed insight into mixing and combustion behavior within an optically accessible rapid compression and expansion machine (RCEM) operated on a split injection PCCI strategy by means of passive optical and laser-optical high-speed diagnostics. In a first measurement campaign, ignition and combustion were characterized by performing combined OH* chemiluminescence, Schlieren and formaldehyde (CH_2O) planar laser induced fluorescence (PLIF) measurements. While from the first appearance of OH* kernels the onset of high-temperature (HT) combustion is determined, CH_2O serves as an indicator for preceding low temperature (LT) fuel oxidation reactions. In a second experimental campaign, TMPD[1] tracer PLIF under inert conditions was used to study the effect of applying multiple injections on pre-ignition fuel-air-mixing. In order to identify a pertinent liquid core and the boundaries of the fuel spray, tracer PLIF was combined with Mie scattering and an additional Schlieren setup. The optical data is used to extract global jet metrics, to explore the influence of varying operational parameters on the in-plane mixing state and to discuss the resulting ignition and combustion dynamics. The analysis of optical data is complemented by a comparison of the jet metrics with literature correlations as well as a comprehensive thermodynamic analysis of global heat release rates and fuel consumption, finally linking the observed findings to engine operation and efficiency.

2 Description of experimental facility

2.1 Rapid compression and expansion machine

The RCEM is a free-floating piston test rig (Fig. 1), originally designed by Testem and further modified in-house (i.e. equipped with a liner heating and modified piston and cylinder head(s)). The RCEM provides excellent optical access and very flexible operating parameters such as compression ratio, charge pressure and temperature. Its modular design allows the custom design of different cylinder heads, which can allows different accesses for diagnostic equipment, windows and injectors depending

[1] n,n,n',n'-tetramethyl-1,4-phenylenediamine

on the needs of the particular experimental campaign. The RCEM used herein is capable of performing a compression and expansion cycle similar to an engine. The working principle of the RCEM is illustrated in Fig. 1, left.

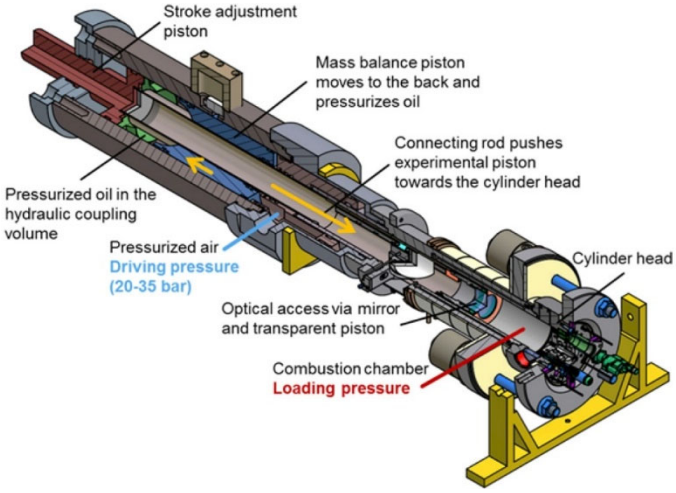

Fig. 1: Schematic view of the RCEM: Pressurized air moves the mass balance piston towards the stroke adjustment piston, accelerating the working piston towards the cylinder head.

Pressurized air moves the mass balance piston, which in turn pushes the working piston towards the cylinder head. The free-floating working piston is accelerated until it approaches top dead center (TDC) and, thereby, compresses the combustible fuel-air mixture. Expanding gases in the combustion chamber are then forcing the working piston back towards bottom dead center (BDC). Both, TDC and BDC are depending on the driving pressure, the charge pressure and the converted energy as well as the combustion strategy. The machine's main bore has a diameter of 84 mm, the maximum stroke can be varied and was set to 245 mm. A solenoid injector with a 100 µm single conical coaxial nozzle was mounted on the cylinder periphery (5 mm below the flat cylinder head, 42.5 mm from the cylinder axis and inclined 5° towards the piston) [1]. The cylinder pressure is obtained with a combination of an absolute pressure sensor in a switch adapter (recording the pressure until 5 bar) and a relative pressure sensor which is pegged during the beginning of the cycle. The cylinder pressure and the piston position are recorded at a rate of 100 kHz during operation. Optical accessibility to the combustion chamber is realized by means of a mirror within the slotted shaft of the working piston (a transparent flat piston bowl with 4 mm depth), a window at the cylinder head (diameter 52 mm) and another window with 40 mm in diameter at the side. A more detailed description of the machine and further operational characteristics can be found in [2-5].

3 Procedures and methodology

3.1 Operating strategy and heat release rate analysis

In order to achieve the desired conditions for PCCI operation with multiple injections, it was found that the most suitable strategy consisted of a comparatively long first injection to provide the necessary base mixture, followed by two short pulses closely spaced to TDC. The operating condition have been selected in order to study cases with different states of mixing at ignition and simultaneously respect the operating limits of the machine. The main goals were to avoid high temperature combustion before the last injection was partially premixed (to avoid mixing controlled combustion, i.e. conventional diesel combustion) as well as to remain within the visible domain, so that mixing and ignition could be observed by the optical diagnostics. n-heptane was selected as mono component surrogate diesel fuel, because of their similar cetane numbers. The fuel injection pressure was set to 600 bar for all operating points (OPs). In case of the non-reactive measurements, the liquid fuel was blended with the TMPD tracer substance at a concentration of 1.5 g/l.

The resulting operating strategy is summarized in Fig. 2. All injection sequences as well as the optical data acquisition were started by a trigger event initiated during the compression stroke as soon as the

accelerating working piston reached a distance of 190 mm with respect to the cylinder head. Unless stated otherwise, time axes within the manuscript are referring to that instance in time. Ten repetitions at each OP were carried out. The top panel of Fig. 2 shows representative time traces of ensemble averaged piston pressure and piston clearance at reactive OP1. Below, the injection schedules and further operational details of the four investigated OPs are summarized. Piston wall temperature and charge pressure were the same for OPs 1, 2 and 4, whereas OP3 featured a slightly elevated charge pressure resulting in a reduced global equivalence ratio. In case of OPs 1, 3 and 4 the same amount of fuel was injected, while for OP2 the energizing time of the first injection was doubled to increase the base load. For OPs 1, 2 and 3, the first base load injection occurred early in the compression stroke, allowing for a prolonged dwell aiming at enhanced premixing, while for OP4 the first injection was delayed by 10 ms. Timing and duration of second and third injections were selected to be the same for all OPs. It has to be noted that due to the free-floating piston design of the RCEM, above modifications to operational characteristics affected the overall compression ratio, which was 10.5 for OPs 1 and 4, 9.9 for OP2 and 8.7 for OP4, respectively.

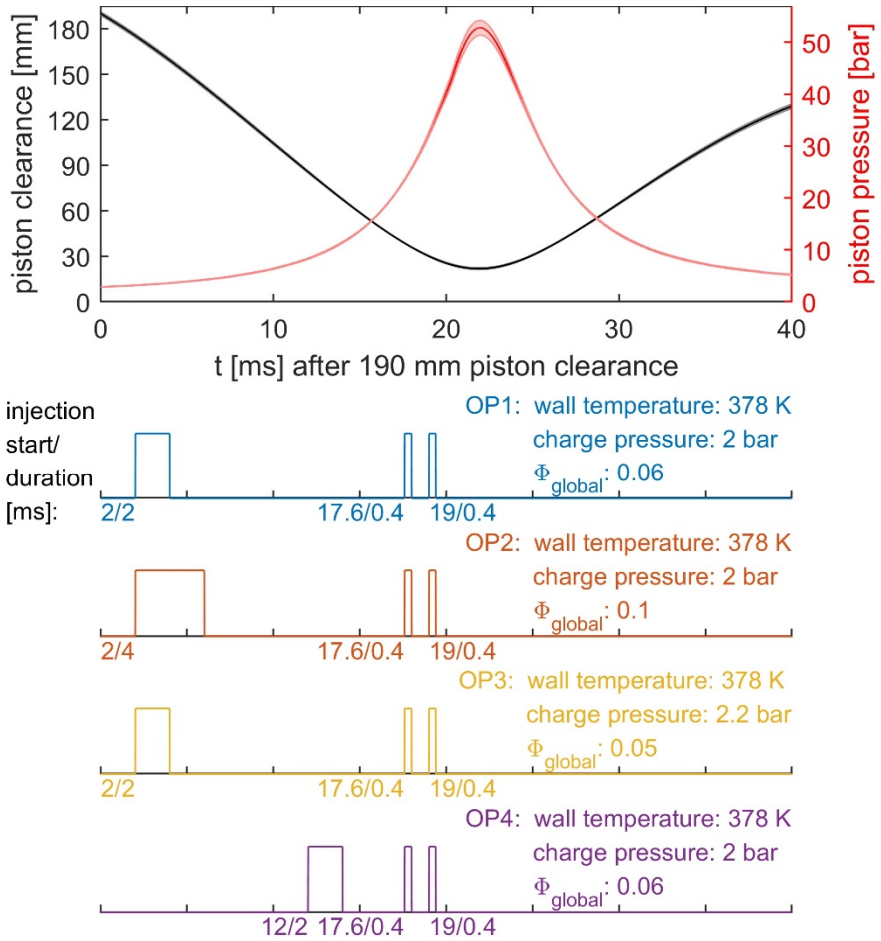

Fig. 2. (Top) Ensemble averaged time traces of piston clearance and pressure at reactive OP1. Shaded areas denote cycle-to-cycle variations of the RCEM. (Bottom) Injection schedules for investigated OPs: Trigger pulses indicate injector energizing times with respect to the start trigger event at 190 mm piston clearance. Respective timings (start of injection/duration) are stated below. Further characteristics for each OP are summarized on the right.

The thermodynamic analysis has been performed with an in-house written software [6], which has already been used in previous works [4, 5, 7]. From the in-cylinder pressure signal and an estimation for heat transfer, the heat release rate was obtained.

3.2 Optical diagnostics

3.2.1 Instrumentation

As indicated above, two successive test campaigns were carried out. In a reactive study, the effect of multiple injections on ignition and combustion behavior were investigated while in a non-reactive campaign, the impact of the split injection schedule on fuel-air mixing was explored. The first setup combined Schlieren, OH^* chemiluminescence as well as CH_2O PLIF imaging, the second Schlieren, Mie scattering as well as tracer (TMPD) PLIF measurements. All measurements were performed out at 10 kHz repetition rate.

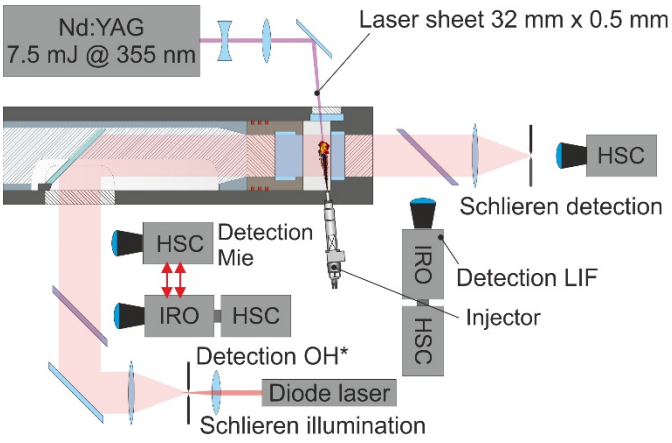

Fig. 3: Optical setup for simultaneous high speed CH_2O -PLIF, Schlieren, and OH*-chemiluminescence imaging (reactive) and TMPD tracer PLIF, Schlieren, and Mie scattering imaging (non-reactive)

Fig. 3 shows a schematic drawing of the optical arrangement. The same Schlieren setup was applied for both reactive and non-reactive campaigns. Schlieren illumination was implemented based on a Cavitar CaviLux Smart diode laser (690 nm, pulsewidth 1 µs). The laser output was collimated by a combination of an aspherical (2", f=40 mm) and a spherical lens (4", f=400 mm). A 4" bending mirror was used to direct the collimated beam into the RCEM. Behind the machine, a second spherical lens (4", f=400 mm) was placed to focus the outgoing laser light onto a circular Schlieren cutoff aperture (diameter ~1 mm). Schlieren images were recorded using a LaVision HSSX camera equipped with a Nikkor VIS lens (f=105 mm, f/2.8).

Both formaldehyde as well as TMPD PLIF signals were excited using the third harmonic output of an Edgewave IS400 high-speed laser at 355 nm. Operated at 10 kHz repetition rate, the laser's output power was about 75 W with a pulse width of 6.5 ns. The laser beam was formed into a collimated sheet of 32 mm height using a combination of cylindrical lenses (f=-25 mm, f=250 mm) and a diaphragm. A 2" dichroic mirror was used to direct the light sheet into the RCEM through the lateral window. The beam waist was adjusted by a third cylindrical lens (f=1000 mm), resulting in a sheet width < 1 mm throughout the visible domain. As indicated in Fig. 3, the light sheet was slightly tilted to match the 5° injector inclination. Since the fuel spray is pushed towards the piston head during the compression stroke, Srna et al. [8] found that the effective symmetry axis of the spray cone has an angle of 3.5°, which was adopted for the arrangement of the light sheet in the present experiments. In both setups, LIF signals were directed towards a LaVision HSS6 high speed camera equipped with a high speed image intensifier (HS-IRO, gate width 150 ns, gain 62) using the same dichroic mirror (4", HR 45 300-450 nm). For CH_2O LIF detection, a Nikkor VIS lens (f=105 mm, f/2.8) and a Hebo color glass filter (B05) were mounted, while in case of TMPD LIF a Sodern Cerco UV lens (f=100 mm, f/2.8) combined with a bandpass filter (Edmund optics, 400±25 nm) were used.

OH^* chemiluminescence was recorded by means of a LaVision HSS6 high speed camera with high speed image intensifier HS-IRO (gate width 75 µs, gain 60), equipped with a Sodern Cerco UV-lens (f=100 mm, f/2.8) and a bk Interferenzoptik bandpass filter (313±7 nm). A dichroic beamsplitter (Eksma,

4'', HR 45 305-320 nm) was used to deflect the back-scattered OH^* signal towards the detection system while the Schlieren laser illumination passed. For the non-reactive tests, in order to detect Mie scattering from the liquid fuel spray excited by the Edgewave laser, the image intensifier was removed and the camera lens as well as the bandpass filter were replaced (lens: Coastal optics, f=105 mm, f/4.5; filter: bk Interferenzoptik, 355±10 nm). Additionally, a different dichroic beamsplitter (CVI, 4'', HR 45 351 nm) was mounted to deflect the back-scattered Mie signal.

3.2.2 Data acquisition and evaluation of optical data

For both reactive and non-reactive campaigns, the start of image acquisition was externally (position) triggered when the working piston reached a distance of 190 mm to the piston head. A second position trigger was used to activate the image intensifier at 60 mm to prevent over-exposure of the intensifier caused by highly fluorescent liquid fuel components pertinent in the 1st injection. At an acquisition rate of 10 kHz, each acquisition channel acquired 400 images and 10 repetitions were carried out at each OP. Since the study focuses on pre-ignition mixing of 2nd and 3rd injection and the combustion behavior near TDC, image processing is limited to time steps 15 ms to 30 ms after the initial trigger event.

In a first evaluation step, all acquired images are mapped to a common grid defined by a transparent dot-pattern target using the LaVision Davis software's built in image dewarping and mapping routines. The origin refers to the injector nozzle tip, the resulting spatial resolution is 0.075 mm/pix. All images are multiplied with a circular mask to account for the viewing windows diameter of 52 mm.

OH^* chemiluminescence measurements are used to asses the onset of auto-ignition as well as the duration of the HT combustion event. Images are background corrected and Gaussian smoothing is applied. Mie scattering data has been carefully examined and it has been found that the core of the liquid jet does not enter the visible range in any operating condition. Therefore, no Mie scattering results are presented. In the following, this section will focus on the more complex evaluation of Schlieren, CH_2O PLIF and tracer PLIF optical data.

Schlieren image processing

In a first step, Schlieren images are flat-field corrected. The flat-field is calculated by averaging the first ten images of each Schlieren image series, whereby the Schlieren signal is still unaffected by the flow and therefore intensity variations exclusively result from the optical setup. In order to extract the contours of the fuel jet, images were further processed by applying an adaptive background subtraction method [9, 10]: The image acquired just before the fuel jet enters the visible area serves as a background image and is subtracted from the subsequent frame. The contrast of the jet area in the background corrected image is further enhanced by applying two-dimensional median filtering, threshold filtering and automated removal of remaining spurious objects, so that eventually the spray contours are obtained as the boundary of the fuel spray area. Jet penetration length and spray angle are then extracted from the spray contours. Finally, the original background image is modified by replacing all image regions outside the jet with corresponding areas from the current frame, while maintaining intensities within the jet boundaries from the previous image. The adapted background image then serves as new background for the next image.

CH_2O PLIF image processing

CH_2O PLIF images suffer from background structures related to spurious light from the Schlieren laser, which is partially reflected by the dichroic beamsplitter. Other background sources involve secondary reflections of the LIF signal and fluorescence exited at the injector head, both illuminating the moving working piston surface. The background is corrected by scaling and subtracting an average background image generated from multiple frames near the end of the acquisition cycle when the formaldehyde fluorescence has disappeared. A second circular mask of 36 mm in diameter is used to remove for remaining piston head artifacts. Finally, Gaussian smoothing and threshold filtering are applied to each image.

Tracer PLIF image processing and transformation to equivalence ratio

The evaluation of the tracer PLIF images is initiated by several image processing steps beginning with moderate Gaussian smoothing of the raw data images. Similar to CH_2O PLIF images, the excited tracer fluorescence causes background artifacts by secondary fluorescence scattering off surfaces. These contributions vary in position and intensity from image to image as they primarily originate from fluorescence emitted by the moving fuel jet. In spatially averaging the current frame in radial direction, an intensity profile reflecting intensity variations along the spray axis is produced. This profile is then scaled and subtracted from each line of the current frame in a trial-and-error procedure, so that erroneous background intensities vanish. A second background artifact arises from a direct reflection of the tracer fluorescence emitted by the fuel jet off the working piston's glass surface. This mirrored portion of the jet is corrected by subtracting an axially shifted and scaled representation of the actual image.

The quantitative interpretation of the processed tracer PLIF images as equivalence ratio fields relies on the procedures outlined in [3, 11, 12]. The interpretation of measured tracer PLIF intensities as equivalence ratio Φ is governed by the following equation

$$\Phi(x,r,t) = \frac{I(x,r,t)}{I_0(t)\, I_{\mathrm{ff}}(x,r)} \cdot \frac{AFR_{\mathrm{stoich}}}{\phi(T)\, K\, \rho_{\mathrm{air}}(p,T,t)}\ , \qquad (1)$$

where I denotes the background corrected PLIF intensity per spatial resolution element (x,r) at time step t. Pulse-to-pulse variations of the laser energy are represented by I_0 and were not recorded during the measurements, since low fluctuation amplitudes below 3 % (rms) were expected based on previous experiments [3]. Due to some unknown reason, the pulse energy varied by 20 % (rms) in the current experiments, which has significant impact onto the measurement accuracy as will be shown below. To account for the efficiency of the acquisition arrangement as well as the spatial distribution of the incident laser light, a flat-field correction is performed: By flooding the combustion chamber with low concentration fuel/tracer vapor and in assuming a homogenous vapor distribution, remaining intensity variations within the field of view can be attributed to the efficiency of the detection devices and the laser beam profile, the latter being assumed temporally constant. A flat-field image I_{ff} is then generated by averaging over an ensemble of 1000 individual images.

While the first expression on the right side of Eq. (1) introduces image operations that are specific to the present setup, the second term contains parameters referring to the conversion to equivalence ratio. The temperature dependent TMPD fluorescence quantum yield is denoted by ϕ and is obtained from an empirical model based on available literature data [10, 13-15]. The bulk piston temperature T as well as the air density ρ_{air} at each time step are calculated from measured piston pressures p in assuming adiabatic compression/expansion. In assuming rotational symmetry of the fuel spray, the proportionality constant K links the injected fuel mass to the volume integrated intensity and is used to transform the quantum yield corrected fluorescence intensity to local fuel density [11, 12]. The operation inherently assumes a low tracer concentration so that absorption of laser energy can be neglected and that the excitation energy of the probed transition stays below the saturation limit. The image at 18.9 ms after the start trigger is selected to perform the procedure, since at this time step the fuel spray of the 2nd injection is visible to its full extend within the camera's field of view. The constant is then used to normalize the respective image series. Finally, the expression is multiplied by the stoichiometric air-fuel-ratio AFR_{stoich} for n-heptane-air mixtures.

Precision of the measured equivalence ratios is analyzed by applying the principle of propagation of uncertainty to Eq. (1). Relevant sources of uncertainty are camera noise, deviation of the fuel jet volume from rotational symmetry and the pulse-to-pulse variation of laser energy. Fig. 4 summarizes the relative precision analyzed for a representative field of instantaneous equivalence ratios, with each symbol representing a single pixel. For values of $\Phi < 0.3$, the precision is determined by camera noise and is, therefore, growing towards lower Φ. At higher equivalence ratios an asymptotic decrease of the resulting precision can be observed, which reaches a minimum value of 23.4 % and is mainly dominated by the 20 % pulse-to-pulse variation of the laser energy. Ensemble averaging over ten repetitions increases the precision by a factor of ~ 3, converging towards 7.4 % for $\Phi > 0.3$.

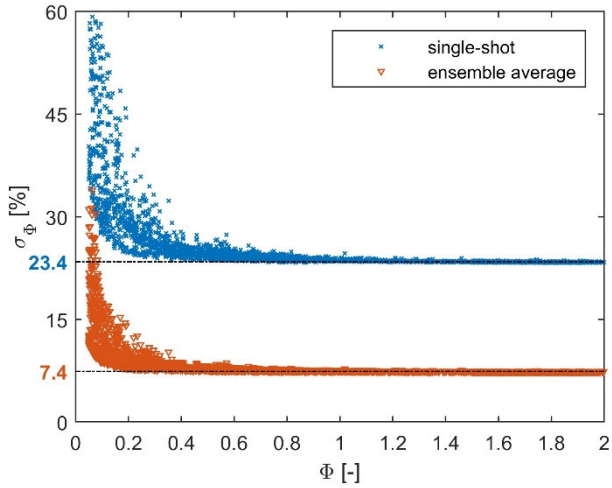

Fig. 4: Single-shot (blue, ×) and ensemble averaged (red, ▽) precision of equivalence ratio.

3.3 Computational Fluid Dynamics methodology

As already mentioned in the introduction section, the interplay of multiphase flow, mixing and chemistry in multi-injection systems is complex and the existing closure models are not suitable for its modeling. Each of the processes needs to be simulated employing as detailed modeling as possible considering the computational resources at our disposal.

In the current study, numerical modeling is conducted by means of Computational Fluid Dynamics (CFD). The detailed geometry of the Rapid Compression Expansion Machine (RCEM) of the Aerothermochemistry and Combustion Systems Laboratory (LAV) at ETHZ is employed in order to reduce the uncertainties related to the volume and pressure near the Top Dead Center (TDC), as well as cavities and crevices prone to the creation of recirculation areas where stratification might occur and affect local reactivity and heat transfer. The tool employed for creating the computational mesh and for solving the discretized problem is CONVERGE version 2.4. This is a versatile tool with excellent meshing capabilities and sufficient level of parallel efficiency and scalability to large numbers of processors. Initial and boundary conditions are selected based on experimental conditions and measurements. The piston motion profile is also based on measurements from the conducted experiments.

In the absence of suitable mixing models, hydrodynamics is modeled employing high-resolution Large Eddy Simulation (LES). More specifically, the one equation eddy-viscosity LES model is employed. It is similar to the classical Smagorinsky SGS model with the difference that the computation of the subgrid turbulence kinetic energy (k_{sgs}) is not assumed to be in local equilibrium and hence an additional transport equation is necessary for the calculation of k_{sgs}. This approach allows for coarser grids and the additional cost of the solution of one more transport equation is covered by the coarser meshing.

The spray is simulated employing a Lagrangian description of the droplets introducing parcels which interact with the surrounding fluid. Heat, momentum and mass transfer occur between the discrete and continuous phases. Each parcel represents a group of identical droplets and the equations for radius, velocity etc. are solved per parcel to reduce overall computational cost. The parcels undergo several physical processes, namely primary and secondary breakup, drag, collision and coalescence, turbulent dispersion and evaporation. All these processes are considered and modelled. Since the first injection occurs early, the fuel enters a low-density environment and hence its penetration is high enough to hit the wall and deposit on the wall in the form of a thin film. This phenomenon is also considered in the simulations by modeling the film creation and evaporation on the walls of the cylinder.

Since hydrodynamics are modeled using high-resolution LES, the grid is fine enough to justify the employment of direct integration of the Ordinary Differential Equations (ODE) constituting the chemistry mechanism. Several mechanisms for n-heptane have been implemented and tested.

3.4 Resolution study

The study carried out, is focused on the first injection of the three existing ones in the base case provided. After analysing the base case and due to the lack of experimental results from the first injection that allow the behaviour of the spray to be validated, study the development of the spray as if it were a free spray is proposed. In parallel, a mesh study is performed considering the real geometry of the RCEM. This analysis is validated using the mesh quality parameters proposed by Celik et al. [48].

3.4.1 Free Spray Analysis

Initially, the free spray study was developed on a 100 mm long cylinder as shown in Fig. 5. Due to the characteristics of the spray, it impacted against the wall and therefore the domain was extended to 150 mm.

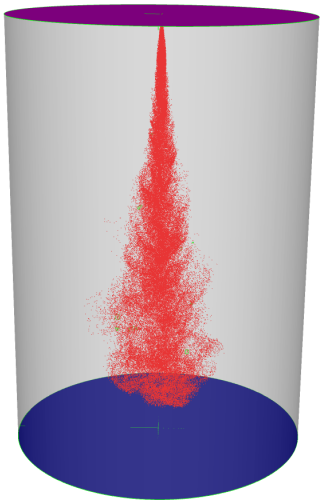

Fig. 5 Domain of 150 mm length for the free spray analysis.

Three different mesh configurations were analysed Fig. 6:

The analysis of the most refined mesh (1mm) includes a cylinder of 1mm around the spray in order to reduce the total number of cells and thus the computational cost.

Fig. 7 presents the results of the previous analyses. Liquid penetrations are very similar to each other whereas a small difference can be seen in the vapor penetrations trend between 1 and 2 ms.

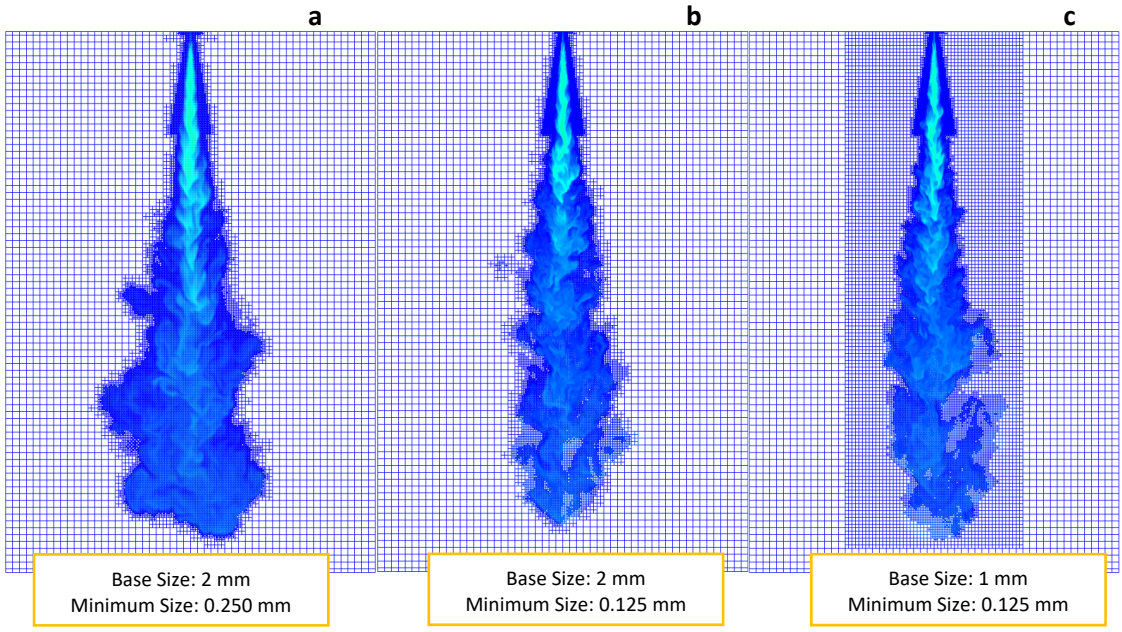

Fig. 6. Mesh analysis. a) 2mm & 3 levels of refinement. b) 2mm & 4 levels of refinement. c) 1mm & 3 levels of refinement.

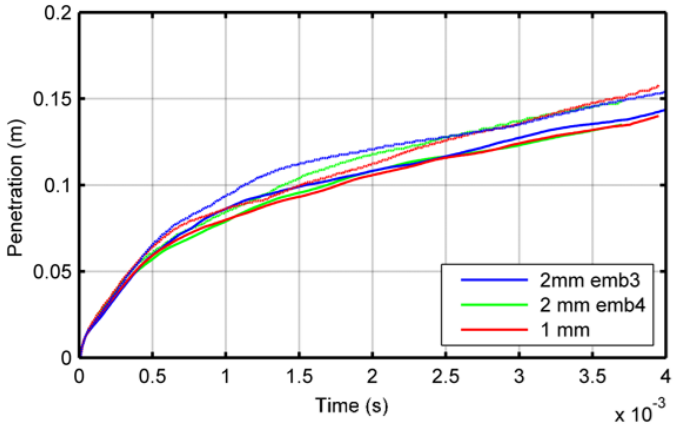

Fig. 7. Liquid and vapor penetrations obtained from the mesh analysis.

Due to the fact that LES models are used for the analysis of turbulence, the quality of the mesh is calculated based on the criteria of Celik et al. [48] in order to determine which mesh ensures enough resolution of the turbulent flow energy (Fig. 8). An appropiate LES quality for High-Reynolds-number flows is guaranteed if at least 75% of the turbulent kinetic energy is resolved.

$$LES_{IQ} = \frac{1}{1 + \alpha_v \left(\frac{s^*}{(1 - s^*)}\right)^n}$$

$$s^* = \frac{\langle \nu_t \rangle + \langle \nu_{num} \rangle}{\langle \nu_t \rangle + \langle \nu_{num} \rangle + \nu}$$

Fig. 8a shows that a mesh with a base size of 2 mm and three levels of refinement leaves part of the spray unresolved. Therefore, a mesh with a higher refinement as presented in Fig. 8b or Fig. 8c should be chosen for a proper analysis.

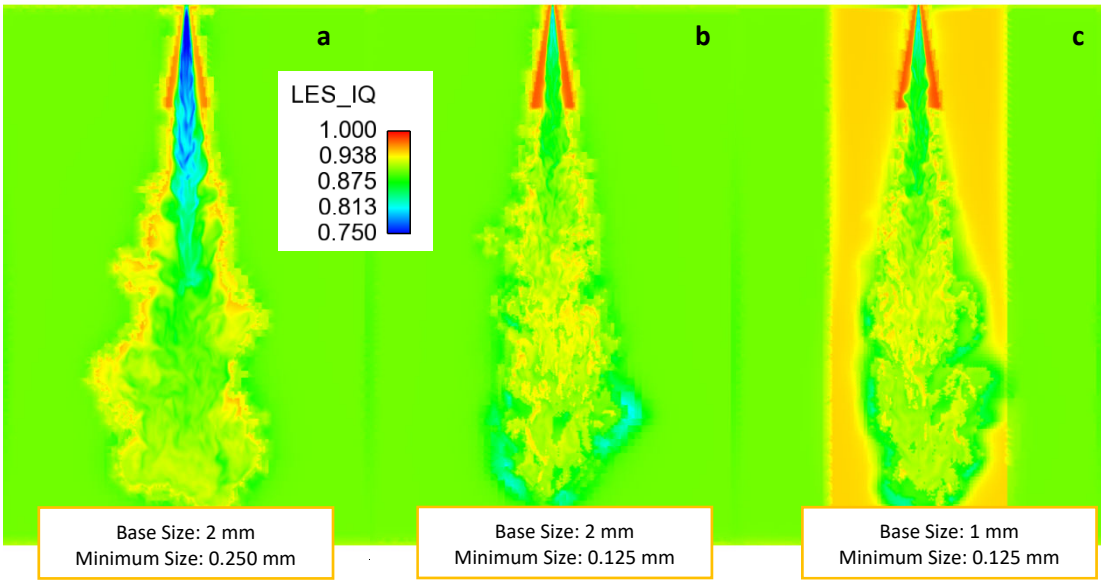

Fig. 8. Mesh quality analysis. a) 2mm & 3 levels of refinement. b) 2mm & 4 levels of refinement. c) 1mm & 3 levels of refinement.

3.4.2 First Injection Analysis. RCEM geometry.

A mesh sensitivity analysis has been carried out using the RCEM geometry and focusing in the first injection. For this purpose, meshes have been compared, their quality has been calculated according to the criteria of Celik et al. [48] and penetrations, velocity and mix fraction have been analysed.

Three different mesh configurations were studied (Fig. 9):

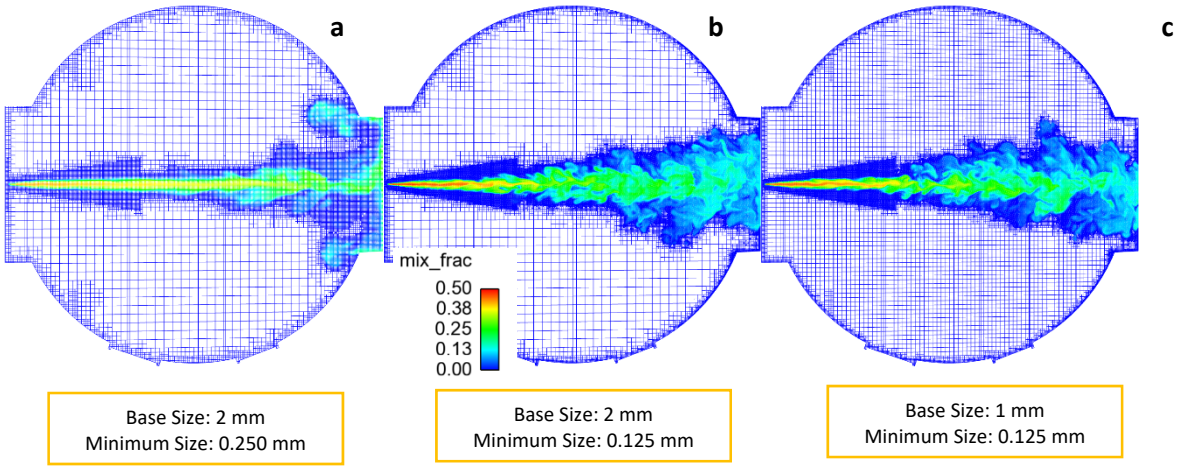

Fig. 9. Mesh analysis in the RCEM domain. a) 2mm & 3 levels of refinement. b) 2mm & 4 levels of refinement. c) 1mm & 3 levels of refinement.

Taking a look at the mesh and the shape of the spray in the case with base size 2 mm and 3 levels of embedding (Fig. 9a), the spray has a similar behaviour as if using a RANS model so the quality of mesh is not sufficient and further refinement is needed. As in the free spray study, cases with an equal minimum cell size behave in a similar way (Fig. 9b & Fig. 9c).

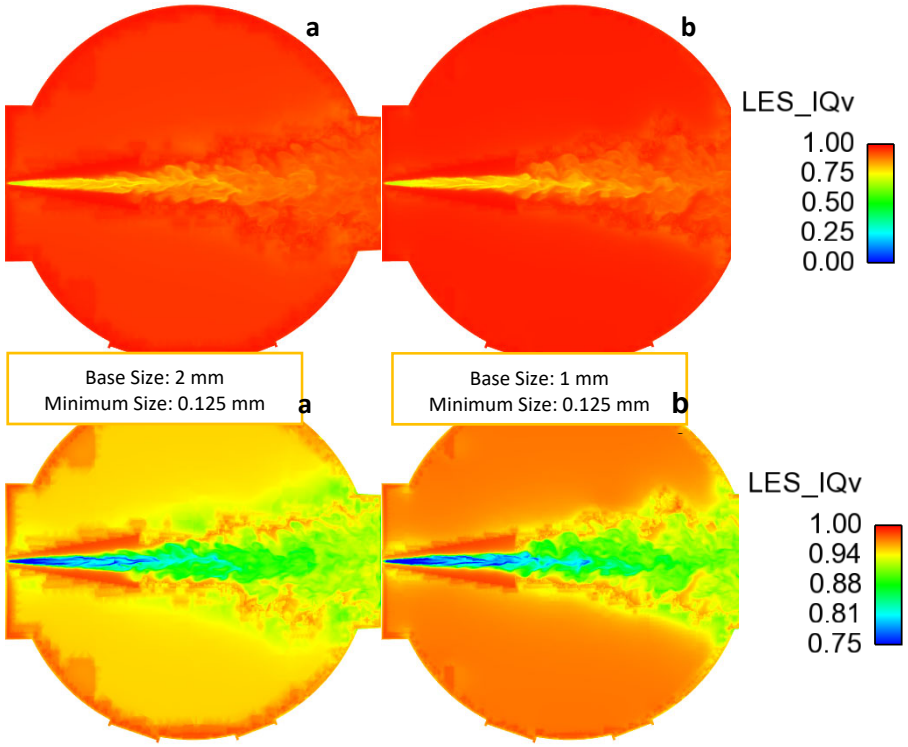

Fig. 10. Mesh quality analysis in the RCEM. a) 2mm & 4 levels of refinement. b) 1mm & 3 levels of refinement.

For the most refined cases, the quality of the mesh has been calculated (Fig. 10). The central part of the spray has cells that do not resolve 75% of the turbulent kinetic energy but do not move too far from that value (~70%).

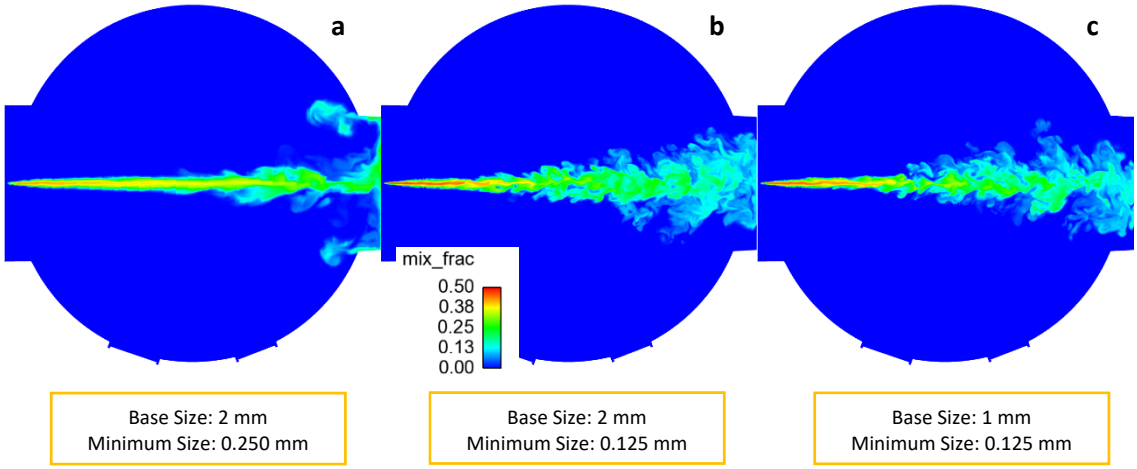

Fig. 11. Mixture fraction results in the RCEM domain. a) 2mm & 3 levels of embedding. b) 2mm & 4 levels of embedding. c) 1mm & 3 levels of embedding.

The more refined cases show a higher amount of mixture fraction (Fig. 11b & Fig. 11c). A greater dispersion of the drops can also be observed, as well as less spray wall interaction at the same time (Fig. 11b & Fig. 11c).

As far as penetration is concerned, the case with a larger minimum cell size (2 mm and 3 levels of refinement) has a greater penetration and therefore impacts earlier on the wall. Furthermore, liquid and vapor penetrations do not show significant differences between them which means that evaporation is quite low. On the other hand, configurations with the same minimum cell size (2mm and 4 levels of embedding & 1mm and 3 levels of embedding) show similar behaviour. All these results above are shown in Fig. 13.

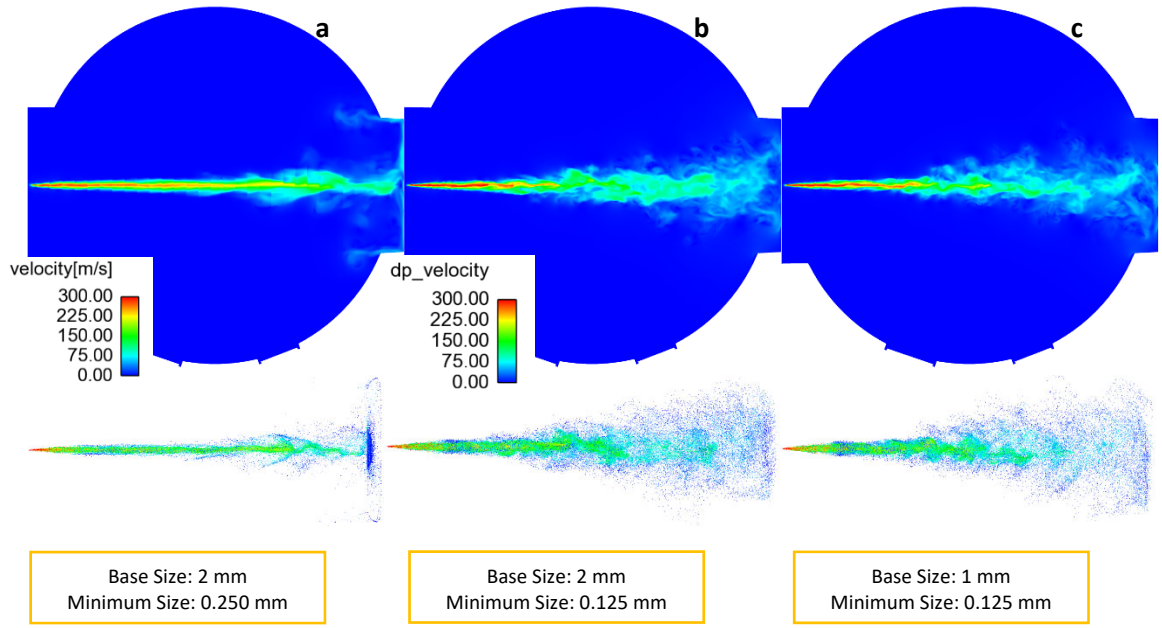

Fig. 12. Velocity magnitude and particle velocity results in the RCEM domain. a) 2mm & 3 levels of embedding. b) 2mm & 4 levels of embedding. c) 1mm & 3 levels of embedding.

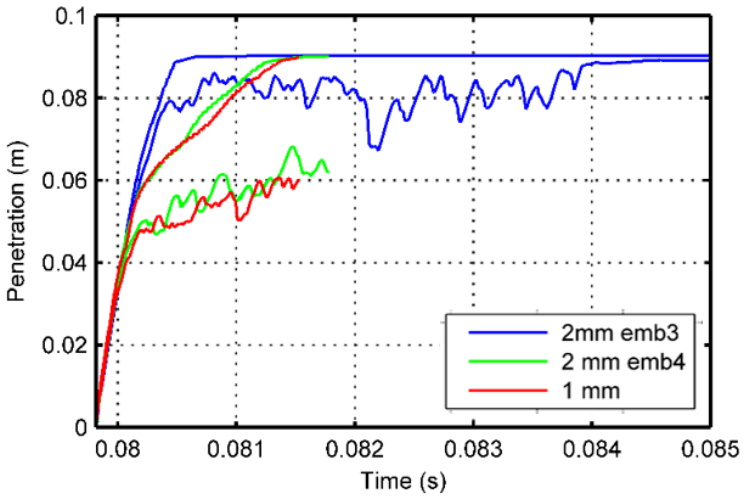

Fig. 13. Liquid and vapor penetrations with different mesh setup.

3.4.3 Computational cost

The simulation setup developed for this study consists of two categories in terms of resolution. The high-resolution setup has minimum cell size of 125μm and maximum cell count around 30 million. The sprays

are resolved with roughly 300’000 parcels and the total computational cost lies between 32’000 and 40’000 CPUhours. The low-resolution setup has a minimum cell size of 250 µm and maximum cell count around 9 million. The computational cost for this case is below 10’000 CPUhours. The complex local interactions between physical and chemical processes dictates the use of high resolution for the production runs. These expensive calculations offer deep insights into the detailed evolution of phenomena that cannot be measured with experimental techniques and hence the information extracted is valuable. The low-resolution setup is used for model testing and for conducting sensitivity studies.

4 Results and discussion

4.1 Jet metrics

The temporal evolution of the jet penetration length and the spray angle of the 2nd and the 3rd injection extracted from the Schlieren contours of the non-reactive measurement campaign are summarized in Fig. 14(left). The injections are of short duration, so that both are completed before the respective fuel spray enters the visible area after ~0.2 ms.

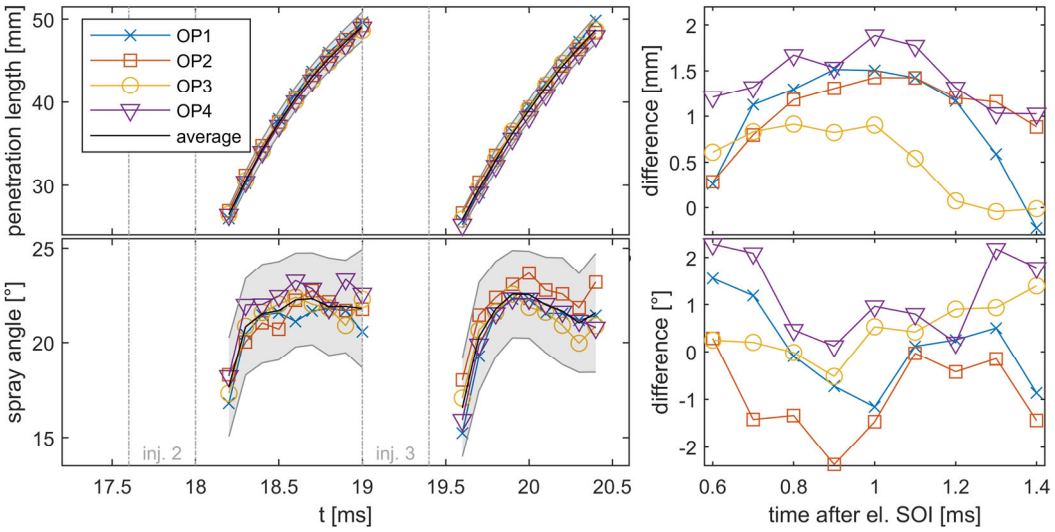

Fig. 14: (Left) Ensemble averaged jet penetration length (top) and spray angle (bottom). Black solid curves represent the respective average over all OPs, shaded areas indicates the average spread over the ten repetitions. Dashed-dotted vertical lines mark the energizing time of 2nd and 3rd injection. (Right) absolute difference of ensemble averaged jet penetration length (top) and spray angle (bottom) of 2nd minus 3rd injection.

The penetration length develops almost identical for all OPs and for both injections. Differences between the curves are well within the experimental spread over the ten repetitions marked by the gray shaded area. The same holds true for the spray angles associated with the 2nd and the 3rd injection, which approach an average value between 21° and 22° when the full width of the spray jet becomes visible within the field of view after ~0.7 ms. From these results it is apparent that the parameter changes according to the operating strategy outlined above have no significant impact on the global jet metrics. In contrast to previously discussed results obtained from optical investigations of multiple injections in CVCs , no faster penetration of the subsequent (3rd) injection is observed in our data. On the contrary, an opposing effect is evident in jet tip penetration differences depicted in Fig. 14 (top, right), leading to decreased penetration rates of the 3rd injection before 1 ms after el. SOI for all OPs. An explanation lies in the transient nature of RCEM ambient conditions compared to CVC experiments: Since the chamber

pressure rises during the compression stroke, the momentum gain caused by the “slipstream” effect is counteracted by the associated density increase and, therefore, results in an overall reduced penetration length instead. At later stages, differences in jet penetration for OPs 2 and 4 stabilize around 1 mm, while in case of OPs 1 and 3 the 3rd injection gains on the preceding jet so that it eventually reaches similar penetration distances. This behavior can be explained by the deceleration of the working piston when approaching TDC, which leads to a significant decrease in density growth rate and, thereby, to a decreasing resistance against the expanding 3rd jet in relation to the expected momentum gain from the 2nd injection. While the penetration length exhibits a pronounced behavior in connection with the engine cycle, no conclusive trends can be deduced from the spray angle data.

Fig. 15 shows in solid the measured penetration length of the spray of OP1 (black 2nd injection, red 3rd injection, similar for the other OPs). The black dashed line indicates the penetration length from a spray model governed by the following equation

$$S = a_0 \sqrt{\sqrt{\frac{P_f - P_a}{\rho_a}} \cdot d_0 \cdot t}\,, \qquad (2)$$

where S is the spray penetration length, a_0 is a parameter to be calibrated and the term under the double square root is the similar to the spray models from [16-18]. P_f and P_a are the fuel respectively the charge pressure, ρ_a is the charge density, d_0 is the nozzle reference diameter and t the time. The parameter a_0 has been calibrated to match the experimental data from the 2nd injection. The red dashed line uses the same model with the same parameter a_0, but with the charge pressure and density evolution from the 3rd injection.

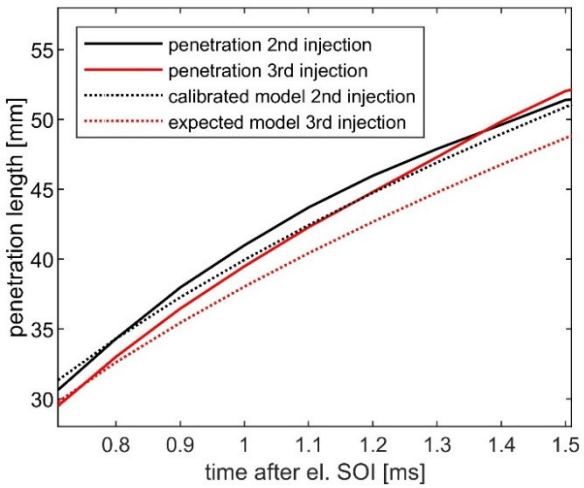

Fig. 15: Ensemble averaged jet penetration length for 2nd and 3rd injection compared with calibrated 2nd and expected 3rd injection derived from Hiroyasu’s model for OP1

The graph shows, that the estimated penetration length for the 3rd injection (red, dashed) differs significantly from the experiment (red, solid). This behavior has already been reported in a constant volume chamber [19], where the penetration of the second of two consecutive sprays penetrates faster due to the discussed aerodynamic effects. However, it is important to note, that in an engine environment, even though the consecutive spray “benefits” from the preceding jet, the penetration does not necessarily need to be faster, since the consecutive spray is injected into a higher pressure and density environment as long as the injection timing is during the compression stroke.

4.2 Mixing dynamics

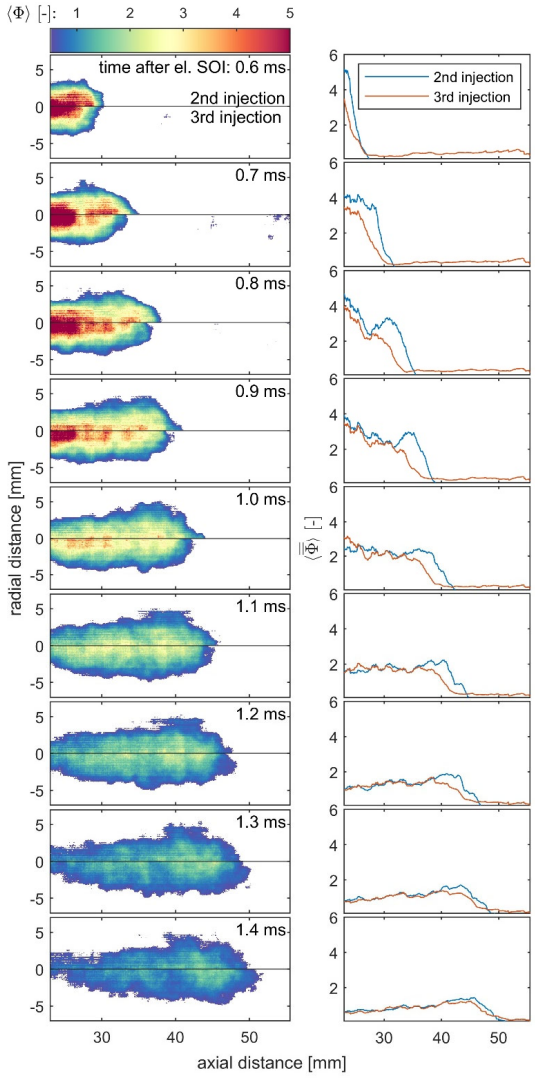

Fig. 16: (Left) Comparison of ensemble averaged equivalence ratio $\langle\Phi\rangle$ maps of 2nd (upper half) and 3rd (lower half) for several time steps after el. SOI. (Right) Corresponding ensemble and cross-sectional average equivalence ratio $\langle\bar{\bar{\Phi}}\rangle$ profiles.

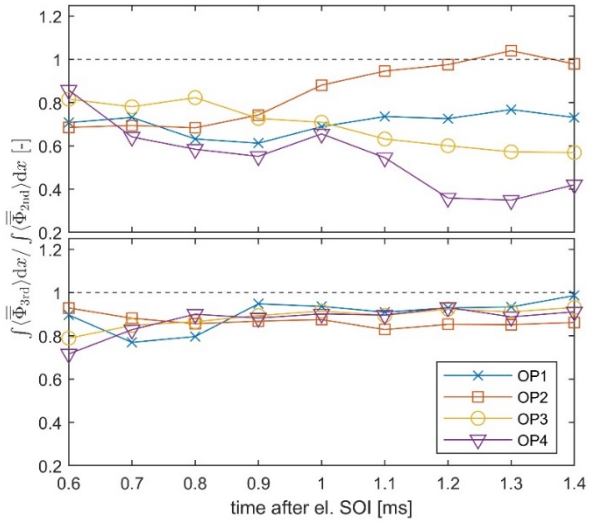

Fig. 17: Ratio of integrated ensemble and cross-sectional average equivalence ratio between 2nd and 3rd injection (top) at the spray head ($x_{\mathrm{tip}} - 5\ \mathrm{mm}$) and (bottom) for the remaining visible spray body.

4.2.1 Local mixing phenomena

The section targets at revealing the complex local mixing dynamics between the 2nd and the 3rd injection and to establish a relation to the matrix of operating points. Owing to the limited precision of the single-shot equivalence ratio maps, the following analysis will rely on ensemble averaged results, denoted by $\langle\Phi\rangle$. Ensemble averaged equivalence ratio maps of 2nd and 3rd injections for OP1 are compared in Fig. 16(left). A threshold of $\langle\Phi\rangle = 0.5$ is used to remove the base load contributions in to enhance the contrast of the jet boundaries.

The mixing fields confirm the faster penetration of the 2nd jet compared to the 3rd injection. Corresponding cross-sectional average equivalence ratio profiles in Fig. 16(right) develop a steep gradient at the spray head of injection 2, which is related to the formation of a stagnation plane and is typical for pulsed jets emerging into a quiescent medium [19, 20]. In contrast, corresponding profiles of the 3rd injection exhibit a significantly smoother decay of the equivalence ratio at the spray tip, indicating enhanced mixing at the head of the post-injection due to the turbulence induced by the preceding jet [19, 21, 22]. The enhanced spray tip mixing of the 3rd fuel jet is further quantified by integrating the ensemble and cross-sectional averaged equivalence ratio of 2nd and 3rd injection at the spray head ($x_{\mathrm{tip}} - 5\ \mathrm{mm}$) and by calculating the ratio between these quantities. Values below unity indicate a faster spray head mixing during the 3rd injection and vice versa. The resulting curves for all investigated operating conditions are summarized in Fig. 17 (top). Until 0.9 ms, ratios are within a range of 0.6 to 0.8, indicating a stable improved mixing rate at the spray head of the 3rd fuel jet for all OPs. While OP1 and OP3 ratios stay within that range for all time steps, OP2 values gradually grow until reaching unity beyond 1.3 ms,

indicating similar spray head mixing rates of the 2nd and the 3rd injection. The OP4 curve instead begins to fall steadily after 1 ms and finally approaches a minimum value of about 0.4. This suggests a continuous increase of the spray head mixing rate of the 3rd injection.As opposed to the markedly different spray head structure of the 2nd and the 3rd injection, the upstream distributions of the ensemble averaged equivalence ratio maps as shown in Fig. 16 (left) for OP1 are of similar shape and magnitude. The corresponding cross-sectional average equivalence ratio profiles confirm this observation by presenting comparable slopes and absolute values in the upstream regions. A comparison of the ratio of integrated cross-sectional average equivalence ratios of the remaining visible spray body in Fig. 17 (bottom) reveals an almost constant offset between 2nd and 3rd injection over all time steps. This leads to the conclusion, that the flow field induced by the 2nd injection results in a stable increase in the upstream mixing rate of the 3rd jet, independent of global parameter changes associated with the operating matrix.

4.2.2 Global mixing state

To analyze the global mixing state, probability density functions (PDFs) from each single-shot equivalence ratio map are produced and ensemble averaged over the corresponding ten repetitions. The results of the analysis are summarized in Fig. 18.

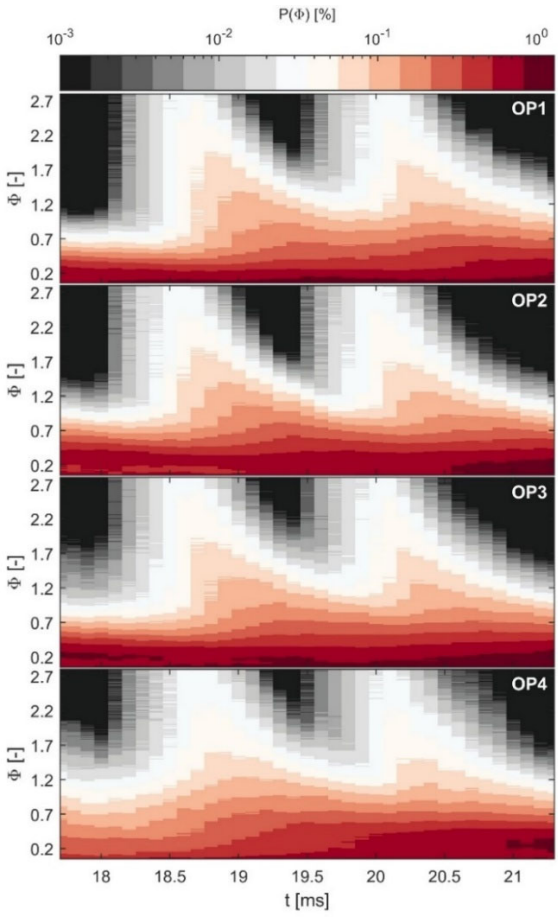

Fig. 18: PDF maps of the light sheet area: Each column represents an average PDF obtained by ensemble averaging the PDFs derived from single-shot equivalence ratio distributions at the corresponding time step. The probability of a certain equivalence ratio (y-axis) to occur at a specific time step (x-axis) is indicated by the color map in logarithmic scale.

Each column of the displayed PDF maps represents the distribution of equivalence ratio within the area illuminated by the laser light sheet at a certain time step. The likelihood of a particular equivalence ratio to occur is indicated by the coloring. At times before 18.1 ms, the distributions show the mixing state resulting from the base load (1st) injection, with all of them displaying a varying degree of stratification. The mixing at OP1 is the most advanced with a maximum probability around $\Phi = 0.2$ and no discernable contributions beyond $\Phi = 1.2$. OP2 exhibits a similar distribution, but slightly shifted to higher equivalence ratios due to the doubled duration of the base load injection. Even though being globally leaner, the mixing state prior to the 2nd injection of OP3 appears even more stratified with equivalence ratios exceeding $\Phi = 1.7$. The increase in stratification might be related to the higher charge pressure and the thereby reduced penetration depth, which changes the mixing dynamics of the base load injection. Finally, the base load stratification is most pronounced in the case of OP4, which is strongly related to the delayed 1st injection and the, therefore, considerably shortened time for fuel-air premixing. Starting with portions of the 2nd jet coming into view at 18.1 ms (0.5 ms after el. SOI), all maps are governed by a peak structure related to the 2nd injection. The steep rise at the beginning points to the wide range of equivalence ratio magnitudes contained in the initial jet. The mixing with the charge, driven by the momentum from the fuel injection leads to rapid decrease in equivalence ratio, resulting in a moderately stratified fuel-air mixture with absolute values below $\Phi = 2.2$. For time steps after 19.5 ms (0.5 ms after el. SOI), the 3rd injection starts to contribute accordingly. Finally, the in-plane mixing state approaches a similar degree of stratification for all OPs.

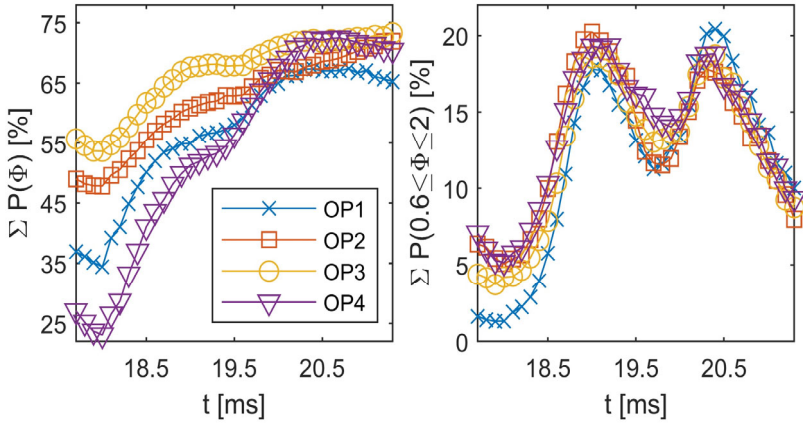

Fig. 19: Accumulated probabilities (excluding zero) $\sum P(\Phi)$ within the light sheet area over all Φ (left) and within the range $0.6 \leq \Phi \leq 2$ (right)

To further investigate characteristics of the global mixing state within the laser sheet area, the accumulated probabilities over all equivalence ratios are plotted against time and compared for all OPs in Fig. 19 (left). The resulting curves reveal, that only a fraction of the probed area is actually filled with fuel-air mixture and that there are pronounced differences between the OPs: While OPs 2 and 3 reach an initial filling state around 50 % and 55 % at 18 ms, respectively, OP1 reduces to 35 % of fuel-air mixture, whereas OP4 drops below 25 %. However, as time progresses, the double injection causes the light sheet plane to gradually fill up until all OPs reach a similar level around 65-70 % of the investigated area.

To give a first implication from the mixing state towards the onset of LT oxidation reactions, Fig. 19 (right) summarizes the accumulated probabilities in the range between $0.6 \leq \Phi \leq 2$ that are prone to initiate a LT combustion event [23]. In contrast to accumulating over all probabilities, confining the analysis to the specified equivalence ratio range results in similar distributions for all OPs. All curves start at a level around 5 % or below, which is followed by a steep growth caused by the contributions of the 2nd injection. After reaching a first maximum around 18.7 ms, leaning of the fuel-rich portions causes the accumulated probability to decrease again. The pattern repeats as soon as the 3rd injection enters

the field of view, until the progression of mixing leaves 10-15 % of the global fuel-air mixture in a state that favors the onset of LT oxidation reactions.

Above findings reveal that, even though there are marked differences in the degree of premixing as well as fuel deposition after the 1st injection, all OPs approach a similar state of mixing after the 3rd injection. This leads to the conclusion, that the in-plane mixing state is primarily determined by the two post-injections, which are identical for all OPs, and not by the applied changes to the operating strategy. Since mixture preparation is essentially the same for all OPs, it is expected that differences in ignition and combustion behavior will be determined by local effects rather than by the global mixing state. This is further shown after analyzing the simulation results in a similar manner as the experimental measurements along the plane coinciding with the spray axis. Very good qualitative and quantitative agreement between experimental measurements and simulated results is achieved, indicating the high quality of the simulation methodology. The global mixing patterns are captured properly and the distribution of the values as well as the temporal evolution of mixing is presented in Fig. 20 for operating conditions 1, 2 and 4.

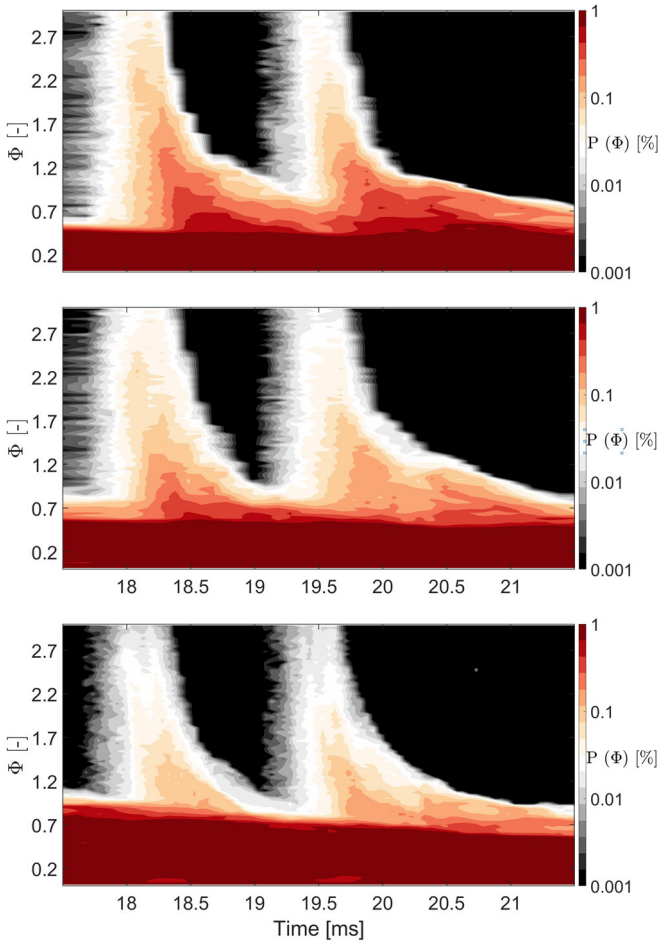

Fig. 20: Temporal evolution of the PDF maps of equivalence ratio. Each column represents an average PDF of equivalence ration along the plane coinciding with the spray axis obtained by the numerical simulations at each time. Top:OP1, Middle: OP2, Bottom:OP4

Regarding OP1 as reference case, OP2 has a larger amount of fuel injected in the 1st injection, OP3 has a higher charge pressure and OP4 a later timing of the 1st injection. OP2, in comparison to OP1 shows a higher absolute amount of fuel burnt and a faster heat release rate. This is due to the richer

base load after the 1st injection. The fuel mass from the 1st injection, which is entrained into the 2nd and 3rd spray and thus forming a flammable mixture is larger. However, also the amount of fuel below the flammability limit is higher. Therefore, the relative amount of combusted fuel is reduced. OP3 in comparison to OP1 has a higher charge pressure and, therefore, a reduced global equivalence ratio. The further reduction of the equivalence ratio also reduces the regions with flammable mixtures and, therefore, the mass fraction burnt. In addition, this operating condition does not show a step in HRR as the other OPs. OP4 in comparison to OP1 has a later timing of the 1st injection, which means that the mixture at the start of the second injection is less homogeneous. This has the consequence that less fuel is entrained into the trailing edge of the second injection (Fig. 19, left). However, a mixture of richer charge is entrained at the tip of the second and third spray (Fig. 19, right), which eventually leads to a larger mass fraction burnt and a steeper HRR.

4.3 Combustion analysis

4.3.1 Thermodynamic analysis and global combustion metrics

Fig. 21 displays the heat release rate (HRR), the total injected energy level and the converted energy for all four OPs. The graphs show trigger to the injector in green, the ten repetitions (black) and the average (red) of the heat release rate on the left vertical axes. In addition, the graphs show the injected energy level (solid) of all three injections and the evolution of heat released in dashed blue with the right hand vertical axes. The percentage of converted to injected energy as well as the global equivalence ratio is displayed in the according subfigure title. The visible 2nd and 3rd injection are always at the same time, with the same fuel pressure and the same duration. The operation conditions only vary in mass and timing of the 1st injection or charge air pressure (according to Fig. 2).

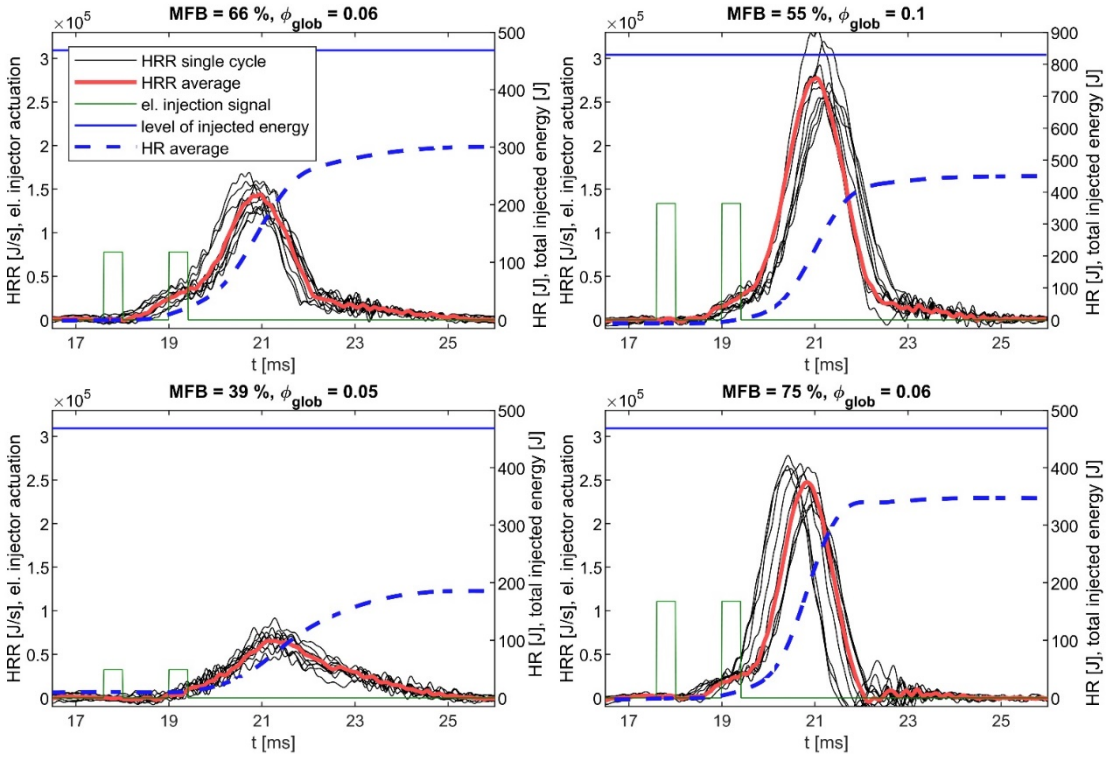

Fig. 21: Thermodynamic analysis: Heat release rate (black (single shots) and red (average)), electronic injection actuation signal (green, left vertical axis), cumulative heat released (blue dashed) and level of total injected energy (blue solid, right vertical axis). Top left: OP 1, top right OP 2, bottom left, OP3 and bottom right OP4.

The results of the ignition and the initial part of combustion extracted from the simulation are in good agreement with the experimentally measured integral heat release (iHR). Although the phenomena are complex and difficult to be modeled, it is shown in Fig. 22 that the evolution of combustion is captured successfully for the cases considered. For operating condition 1 (OP1), the simulation predicts a delay in ignition of about 1 ms compared with the experimental measurement. Ignition in OP3 is less accurately predicted since the difference between simulation and experiment is almost 2 ms. The rest of the cases show lower ignition delay, the late ignition timing compared to experimental measurements is consistent for all of them. This is attributed to the limitations of the chemical mechanisms at the low temperature limit and their inaccuracy in predicting CH_2O production early enough during the low temperature combustion regime. Specific to OP3 is the piston motion profile, which is an input for the simulations. Uncertainties in the piston motion profile result in significant differences in the predicted combustion evolution.

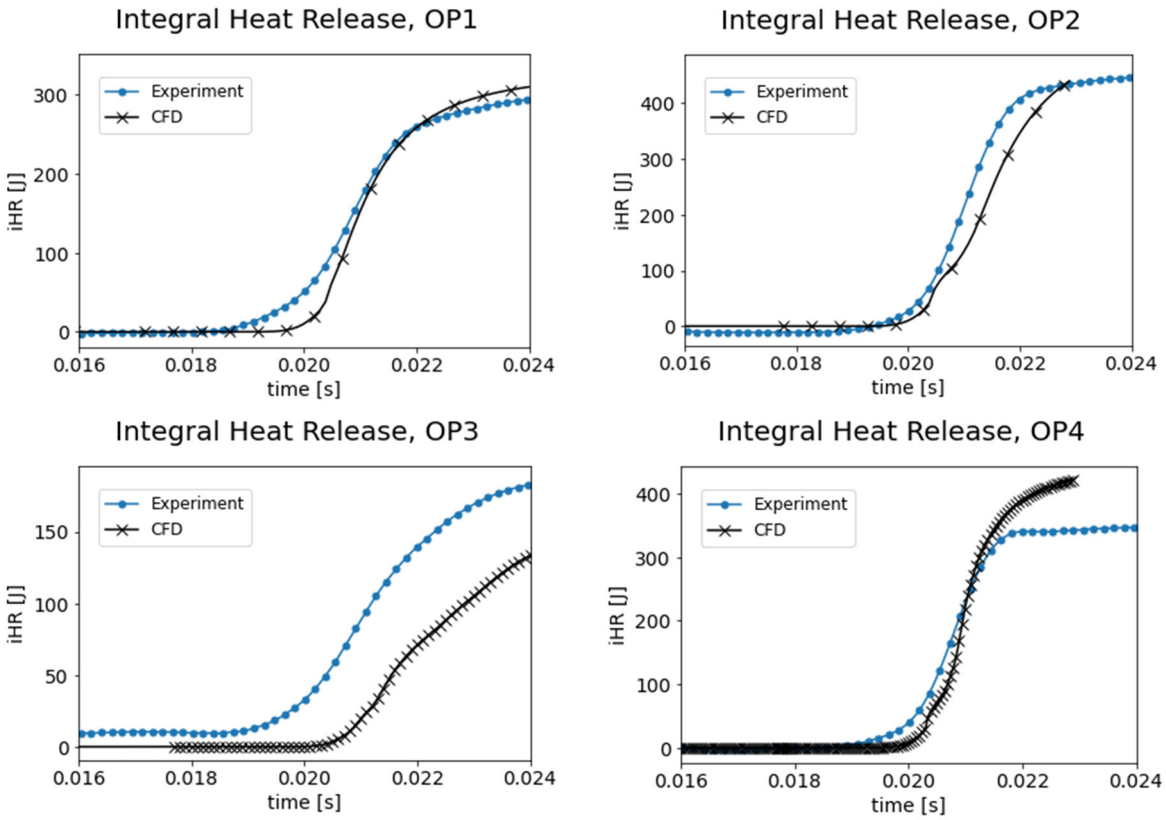

Fig. 22. iHR as a function of time after the start of measurement for all the operating points considered

Fig. 23 compares the relevant timings from the thermodynamic analysis and the global optical metrics (i.e. start and end timing of the OH^* signal the CH_2O PLIF signal, representing formaldehyde). The figure shows in blue, orange and yellow the start, 10% and 90% point of the total heat released, in green and light blue the start and end of the OH^* signal and in purple and red the start and end of the formaldehyde signal. The vertical axis is the time and the horizontal axis represents the four OPs. The thermodynamic begin of the HRR is the earliest detected value in all cases. The start of formaldehyde lies between start and 10% of the total heat released. The reason to see the two signals not on top of each other is that the formaldehyde signal is only visible inside the light sheet plane. The reactions outside this plane are not detected. In addition, the CH_2O PLIF signal was contaminated with background artifacts, which, although corrected, decrease the signal-to-noise ratio and thereby raise the lower detection limit. On the other hand, the start of the OH^* signal matches the 10% heat release for three of the four OPs. This

means, that 10% of the HRR are already converted in LT combustion before the onset of HT combustion. For OPs 1, 2 and 4, the HRR in Fig. 21 also shows a significant change in rate at roughly 20 ms. The 90% point of the heat released matches quite well with the end of the OH^* signal. However, the temperatures are still high and the available fuel under very lean conditions is still being converted in the LTC regime. The end of the formaldehyde signal is significantly later. For OPs 1, 2 and 3, the HRR in Fig. 21 is still visible after roughly 22 ms. For OPs 1 and 2, a significant change of rate is visible, whereas in OP3, the difference between LT and HT combustion is too weak. OP4 shows no significant HRR after 22 ms, and the formaldehyde signal ends first of all OPs. Additionally, OP4 is the operating condition with the highest fuel mass fraction burnt.

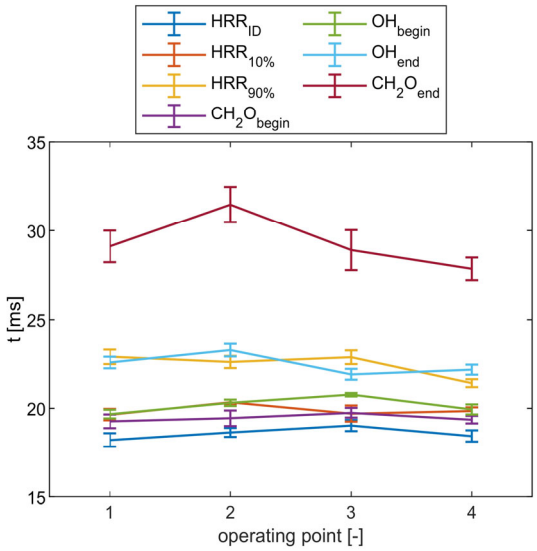

Fig. 23: Global combustion metrics: Ignition, 10% and 90% cumulative heat released (relative to the converted and not to the injected fuel, dark blue, orange and yellow), start and end of formaldehyde appearance (purple and red), start and end of OH* appearance (green, light blue)

4.4 Ignition characteristics

Auto-ignition of high-pressure fuel sprays is a complex process that depends on the local history of the fuel-air mixture, combustion chemistry and the interaction between flow and reaction kinetics [23, 24]. In this context, global changes of operating parameters such as injection timing or charge pressure have a multi-dimensional effect on these local conditions, so that even small variations of the operating strategy can have a significant impact on the local ignition behavior. Additional operative degrees of freedom are introduced by the RCEM design used herein, where, due to the free-floating piston, the long 1st injection of OP2 as well as the increased charge pressure of OP3 impact the compression ratio and thus alter the temperature rise rates and peak temperatures during the compression stroke. Both the RCEM specific engine cycle as well as the local impact of global parameter changes find their expression within the global combustion metrics in Fig. 21.The following analysis aims at disentangling some of these effects.

The characterization of the ignition behavior in relation to the operating strategy relies on a combined analysis of high-speed Schlieren, CH_2O PLIF and OH^* chemiluminescence measurements. At that point it must be stressed that the following analysis is naturally restricted to the optically accessible part of the RCEM combustion chamber, which does not exclude HT or, in particular, LT oxidation reactions to occur outside the visible domain. Schlieren and OH^* chemiluminescence images contain line-of-sight integrated information, whereas CH_2O PLIF is localized to the laser light sheet plane, which, furthermore, does not exclude LT reactions to take place outside this plane but inside the visible area.

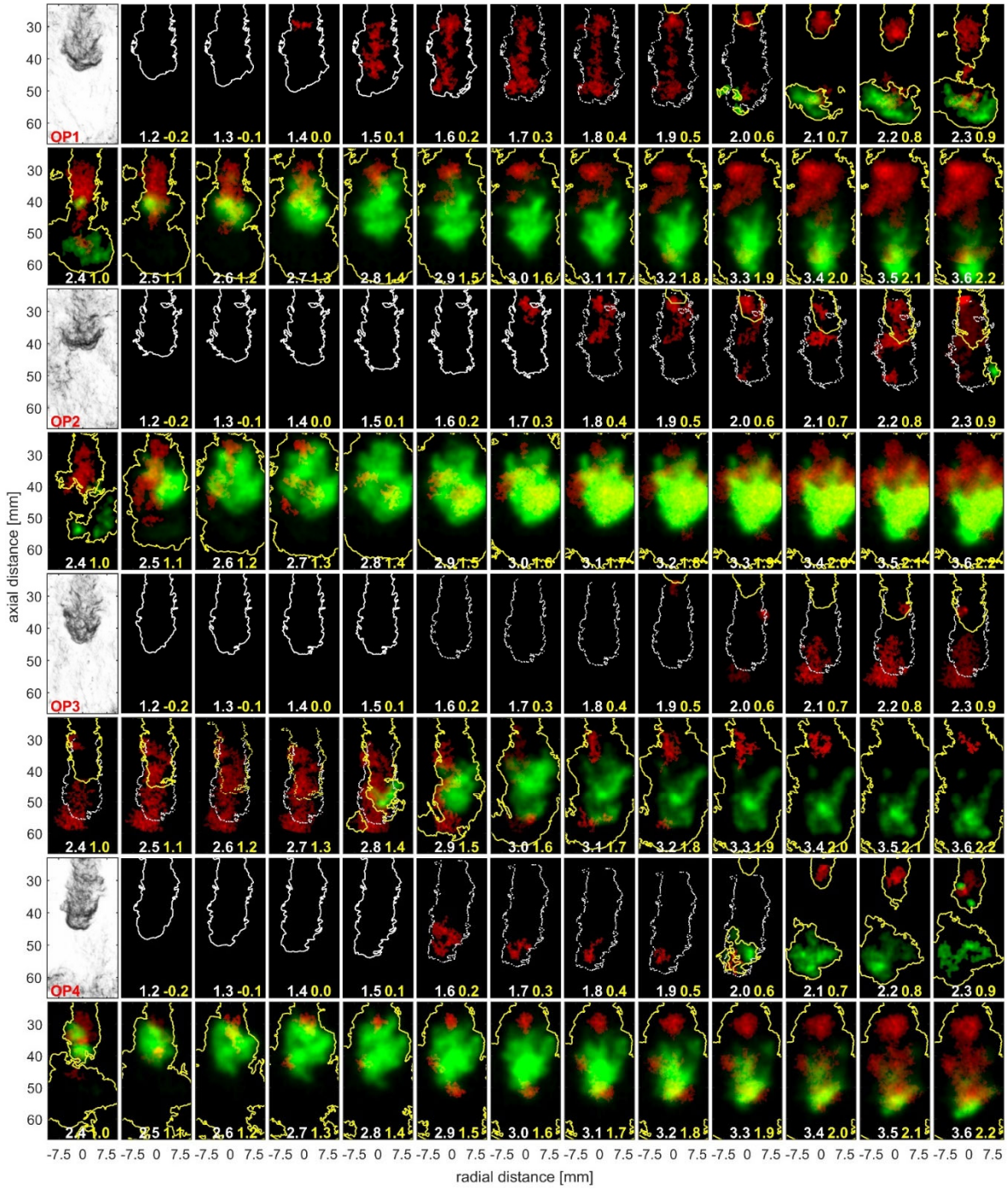

Fig. 24: Time-resolved ignition dynamics: Each OP occupies two rows and is introduced by a Schlieren image. Subsequent images contain the simultaneously acquired in-plane CH_2O PLIF signal (red) and the line-of-sight integrated OH^* chemiluminescence (green). Superimposed are the jet contours of 2nd (solid white) and 3rd injections (solid yellow) extracted from the simultaneously acquired Schlieren image data. Jet contours become dotted when tracking in the Schlieren data is no longer feasible. The last detectable contour is kept and translated along the jet axis by an amount related to the average jet tip velocity extracted from the non-reactive Schlieren data. Numbers at lower right denote the time after el. SOI_2 (white) or SOI_3 (yellow) in ms.

Representative sequences of the ignition behavior for a single measurement run out of the ten repetitions for each OP are summarized in Fig. 24 Regarding OP1, a first spot of formaldehyde within the 2nd fuel spray is formed 1.4 ms after el. SOI_2 about 30 mm downstream from the nozzle tip. At that time step, the mixing state appears to be ideal to promote LT ignition since the local equivalence ratio, due to fast mixing at the trailing edge of the spray results in higher temperatures then in richer conditions towards the spray tip [25] (Fig. 24, right). In addition, the global structure of the mixing field (Fig. 19, right) exhibits large portions of equivalence ratio ($\Phi < 2$) prone to undergo LT oxidation. The first LT ignition spot then grows rapidly in the downstream direction to finally cover the entire span of the 2nd fuel jet at 1.8 ms. When the head of the 3rd fuel spray comes into view at 1.9 ms after el. SOI_2, the LT reactivity related to the 2nd injection already appears to decline, until at 2 ms only small portions at the spray head remain. At the same time, however, first HT ignition kernels appear at a similar axial location between 50 and 60 mm and merge into a single reaction zone, which then expands over several time steps, is transported downstream and disappears again 2.5 ms after el. SOI_2. In contrast to the 2nd injection, the 3rd fuel spray exhibits a distinctly different LT ignition behavior, as portions at the spray head immediately undergo LT oxidation reactions 0.6 ms after el. SOI_3. The shortened LT ignition delay between 2nd and 3rd injection agrees well with earlier observations and is related to the entrainment of hot LT reaction products from the preceding by the subsequent jet [19, 22]. In addition to this established explanation, the enhanced mixing at the head of the 3rd spray due to the slipstream effect leads to leaner mixtures in comparison to the rich stagnation plane structure of the 2nd jet (compare Fig. 24, right at 0.9 ms), which are more susceptible to undergo LT oxidation reactions. Formaldehyde fills the cross-section of the 3rd jet, until at 1 ms after el. SOI_3, a HT ignition kernel related to the arrival of the 3rd injection develops 40 mm downstream from the injector nozzle. In the following time steps, the HT ignition kernel expands in all directions and partially consumes the formaldehyde. The HT reaction zone reaches its maximum extend at 1.4 ms after el. SOI_3 and is then transported in downstream direction, whereby an intense formaldehyde signal develops in its wake. A similar observation of post-combustion formaldehyde was also made in [19] and is related to an incomplete consumption of the available fuel during the HT reaction. The higher intensity of the post-combustion CH_2O PLIF signal, however, does not necessarily indicate a higher LT reactivity and should be interpreted with caution. Even though high pressure and temperature after HT combustion promote quenching of the formaldehyde fluorescence [26], this is counterbalanced by the absence of oxygen, which is found to have one of the highest quenching rates for formaldehyde [27]. In this context, since ambient conditions after HT combustion appear overall favorable to sustain LT reactivity, the remaining fuel partially undergoes LT oxidation reactions, which, however, do not proportionally contribute to the combustion efficiency (compare Fig. 21).

LT reactivity of OP2 starts about 0.3 ms after OP1, however, at a similar axial location within the boundaries of the 2nd fuel spray. One time step later at 1.8 ms after el. SOI_2, the initial spot has grown in axial direction until it covers about half of the jet's cross-sectional area. In contrast to OP1, no LT reactivity occurs in the jet's downstream half until 2 ms after el. SOI_2, where a first formaldehyde spot emerges near the spray head. At 2.3 ms after el. SOI_2, LT oxidation reactions finally occupy a substantial part of the downstream half of the 2nd fuel spray. The explanation both to the delayed onset of LT oxidation reactions as well as the postponed LT reactivity in the jet's lower half in comparison to OP1 is twofold: First, the lower compression ratio results in a reduced rise rate of the ambient temperature, so that it takes longer to trigger LT reactivity. Second, the higher base load leads to richer mixtures, such that in the lower half of the 2nd spray the equivalence ratio is still too high (and temperature is too low) to undergo LT oxidation. In accordance with the time delay of 0.3 ms to the beginning of LT reactivity and at a similar axial location compared to OP1, a first HT ignition kernel is formed 2.3 ms after el. SOI_2 near the tip of the 2nd fuel spray of OP2, spreads slightly and loses intensity rapidly in the following time steps. Other than OP1, the LT reactivity of the 2nd fuel spray is still on-going when the 3rd jet enters the visible domain 0.5 ms after el. SOI_3 and seems to be partially quenched at 0.7 ms due to colder portions of the 3rd spray mixing with the LT combustion products of the 2nd injection. The 3rd fuel spray further expands and quickly fills with formaldehyde, until it reaches the outline of the HT reaction zone of the 2nd jet 1 ms after el. SOI_3. In contrast to the initially small and then gradually growing HT ignition kernel development of OP1, a large HT reaction zone appears centered around that area. The HT reaction

zone rapidly grows in size and intensity as it consumes the upstream mixtures and, unlike OP1, remains in a fixed location for several time steps. When transported downstream with the flow, the size of the reaction zone decreases slightly but with still growing intensity. Similar to OP1, the incomplete fuel consumption during HT combustion leads to post-combustion LT reactivity developing throughout the visible area.

In case of OP3, both LT and HT ignition deviate significantly from the previously described behavior of OPs 1 and 2. As a reminder: Due to the increased charge pressure, OP3 has the lowest global equivalence and compression ratio, the latter resulting in reduced compression temperatures per time step. The latter leads to a significant delay of LT reactivity of the 2nd injection until 2 ms after el. SOI_2. Unlike OPs 1 and 2, where first LT oxidation reactions are located in the downstream half of the 2nd jet, the initial LT reactivity of OP3 appears at the tip of the 2nd spray at an axial distance between 50 and 60 mm from the injector. This is due to the fact that, as soon as ambient temperatures are sufficiently high to trigger LT reactivity, the upstream mixing is further advanced so that mixtures are too lean, while equivalence ratios at the spray head have reached a level suitable to promote LT oxidation reactions. In the following, LT reactivity spreads in the upstream half of the 2nd spray, but without HT ignition to occur. In contrast to OPs 1 and 2, where the incoming 3rd injection immediately undergoes LT oxidation reactions, the absence of LT combustion products from the 2nd fuel spray fails to trigger LT reactivity inside the boundaries of the 3rd jet (small spots from 0.5 to 1 ms after el. SOI_3 are most likely background artifacts). The 3rd fuel spray eventually undergoes LT oxidation reactions 1.1 ms after el. SOI_3 and merges with the still persisting LT reaction zone of the 2nd jet. The onset of HT combustion then occurs 1.4 ms after el. SOI_3 at the head of the 3rd fuel spray and from there, the reaction zone quickly expands in the upstream direction. The resulting HT reaction is less intense compared to OPs 1 and 2 and its location is less persistent, so that it rapidly extinguishes when transported downstream with the flow, leaving a reduced LT reactivity in its wake. Both the decreased intensity and duration of the HT combustion event as well as the lowered pre- and post-combustion LT reactivity explain the very low MFB of OP3 with 39 % of the injected fuel mass only.

OP4 in comparison to OP1 faces the same amount of total fuel injected and is operated with the same charge. However, the timing of the 1st injection is delayed. This leads to a different mixing pattern. According Fig. 19 left, only 25 % of the light sheet plane are filled with fuel-air mixture prior to the 2nd injection. However, these 25% are more fuel rich because the1st fuel spray has less time to mix (Fig. 19 right). This means that less fuel is entrained by the 2nd jet in the upstream regions of the spray, thereby leading to lower equivalence ratios in the upstream regions. The lower equivalence ratio in comparison to OP1 in this region is not expected to influence the local temperature due to the comparably large dwell between 1st and 2nd injection. With similar local temperature fields and richer conditions, the LT reactions of OP1 are occurring earlier and further upstream in comparison to OP4. Similar to OP3, first LT oxidation reactions are, therefore, shifted to the head of the 2nd spray, however, occur already 1.6 ms after el. SOI_2. Since the compression ratio of OP4 is considerably higher than that of OP3, the resulting increase in ambient temperature promotes LT reactivity at the comparably rich spray head region at a much earlier stage, while the upstream portions of the spray are still too lean to ignite. In the following, LT reactions are restricted to the head of the 2nd spray and do not spread further upstream, until auto-ignition occurs at a similar location 2 ms after el. SOI_2. The resulting reaction zone consumes the combustible mixture in the spray head region and extinguishes quickly 2.4 ms after el. SOI_2. Even though LT combustion products are absent in the near nozzle region, unlike OP3, high temperatures due to the elevated compression ratio and the already started HT combustion of the 2nd jet provoke LT reactivity within the limits of the 3rd jet immediately after it becomes visible. This is quickly followed by two auto-ignition kernels emerging between 30 and 40 mm downstream from the nozzle, which gradually grow into a single expanding reaction zone. The then progressing HT combustion event is very similar in intensity and duration to OP1 and eventually leaves a post-combustion formaldehyde signal in the wake of the downstream transported HT reaction zone.

To further substantiate above findings, LT and HT ignition timings as well as ignition locations are analyzed for all measurement runs and combined with respective results of the ensemble averaged mixing field. Although rising temperatures with respect to LT fuel oxidation will lead to local expansion

of the flow field and thus change the local equivalence ratio distribution, it is argued that the following results nevertheless will display the qualitative trends in relation to the operating strategy. Fig. 25(a) and (b) show equivalence ratios averaged over the initial LT ignition zones and their mean axial distance from the injector plotted against the LT ignition timing. Average equivalence ratios at LT ignition are all on similar levels and, with corresponding values for OPs 1 and 4 as well as slightly higher and lower magnitudes for OPs 2 and 3, follow the operating strategy. Likewise, the LT ignition timings are dominated by the varying compression ratio and the associated differences in ambient temperature, so that OPs 1 and 4 have a similar LT ignition delay, while LT oxidation reactions of OPs 2 and 3 are delayed. The average axial distances of the LT ignition event from the injector nozzle in Fig. 25 (b) confirm the trends found in the time-resolved analysis, whereby OPs 1 and 2 start LT oxidation reactions between 30 and 40 mm and OPs 3 and 4 further downstream around 50 mm. This distinct behavior is associated with the local structure of the mixing field: Even though differences in equivalence ratio at the location of LT ignition are small, the entrainment of base load fuel by the 2nd injection leads to richer fuel-air mixtures, so that in case of OPs 1 and 2 the ignition location moves further upstream where mixing conditions are favorable to support LT oxidation reactions. The 2nd fuel spray of OP3 entrains base load mixture as well, however, mixtures in the upstream part of the jet remain too lean so support LT reactivity, so that the LT ignition is shifted to the richer spray head region. Regarding OP4, the absence of base load fuel due to the late 1st injection results in leaner conditions within the boundaries of the 2nd spray. Therefore, the equivalence ratio in the upstream jet is too low to trigger LT oxidation reactions, so that the initial LT reactivity occurs at the richer spray head.

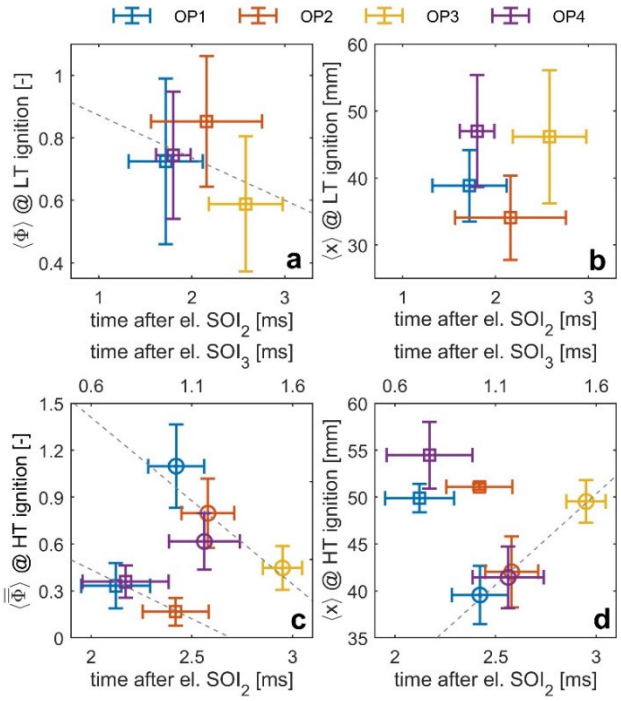

Fig. 25: Ignition statistics: Spatially averaged (a) equivalence ratio and (b) axial distance from the injector at LT ignition locations plotted against LT ignition delay. (c) Cross-sectional average equivalence ratio and (d) axial distance from the injector at HT ignition locations plotted against HT ignition delay related to SOI 2nd (bottom x-axis) and 3rd (top x-axis) injection. Symbols □ and ○ are used to discriminate between ignition events related to 2nd or 3rd injection, errorbars indicate the spread of the corresponding variable over the ten repetitions. Dashed grey lines show respective trends and are inserted to orient the reader.

A similar analysis is performed for HT ignition in Fig. 25 (c) and (d). In order to link HT ignition timings to the local mixing state, planar equivalence ratio fields measured by tracer PLIF cannot be used right away, since the depth position of the in-plane fuel-air distribution does not necessarily correspond to that of an ignition kernel in the line-of-sight integrated OH^* chemiluminescence signal. However, as the axial coordinates of OH^* chemiluminescence and mixing field are the same, cross-sectional average equivalence ratios can be used for that purpose instead. As discussed above, the HT ignition of OPs 1, 2 and 4 can be separated in two distinct events related to the arrival of the 2nd and the 3rd fuel spray. This is indicated by the square (2nd) and circle (3rd) symbols and the upper and lower time axis in relation to SOI_2 and SOI_3, respectively. In case of OP3, HT ignition is characterized by a single ignition event only. When comparing ignition delay and local mixing state between the two HT events for OPs 1, 2 and 4, the first ignition occurs at very lean conditions with ignition delays twice as long, which is well in line with previous findings in the literature [19, 28]. It is visible, that the HT reactions in contrast to the LT reactions show a stronger dependency on the equivalence ratio, which is in agreement with previous works for mixtures of hydrocarbon fuels with air [1]. In particular, this is visible in the second HT ignition event, which is significantly influenced by flow and chemistry related mechanisms: OP1 has the shortest second HT ignition delay and ignites at the smallest axial distance. This behavior has its origin in an increased upstream LT reactivity within the 2nd fuel spray, which generates hot reaction products that are entrained by the expanding 3rd injection, combined with a relatively high compression ratio and, thus, ambient temperature. In terms of upstream LT reactivity, the 3rd injection of OP2 experiences similar conditions compared to OP1. However, as ambient temperatures are reduced due to the lower compression ratio, the second HT ignition event is slightly delayed and is located further downstream in a leaner mixing state. OP4 on the other hand has similar ambient conditions compared to OP1, but lacks the upstream LT reactivity of the 2nd fuel spray, leading to a similar second HT ignition delay, position and mixing state compared to OP2. Finally, due to the low compression ratio combined with the leanest fuel-air mixtures, HT ignition of OP4 is significantly delayed and shifted downstream. As indicated by the lowest MFB of 39 %, significant portions of the fuel-air mixture stay below the flammability limit.

The experimental results and findings were successfully published in FUEL [29].

4.5 Detailed analysis of simulated ignition processes

One of the advantages of CFD is the creation of detailed datasets, both in terms of spatial and temporal information, of every variable relevant to the analysis of the phenomena under investigation. In order to analyze the ignition processes and investigate the effect of multiple injections on mixing we define three different mixture fractions, each one corresponding to the three different injections. This kind of information cannot be retrieved by means of experimental measurements and hence the employment of CFD offers useful additional information and insights on top of the experimental efforts.

The spatial and temporal evolution of the mixing processes and the effect of each of the three injections for OP1 is presented in Fig. 26 as contour plots on the slice defined by the plane parallel to the injection. The mixture fraction corresponding to the fuel injected during the first injection is colored in black, the one corresponding to the second injection in blue and finally the mixture fraction corresponding to the third injection is colored in green. The mass fraction of formaldehyde, which is used as an indicator of ignition is colored in red. The superposition of all the above-mentioned quantities are presented in the two upper rows of fig. 26. The lower rows of this figure show the temperature contours and the dark red spots indicate locations of high temperature combustion. It is observed that there is increased concentration of fuel in the near wall region due to the early first injection impinging the walls at high velocity. The first spot of increased CH_2O mass fraction is located at a region which is dominated by fuel injected during the second injection and subsequently we see that CH_2O is produced in pockets of fuel injected either during the second injection or in the areas of mixing of the second and the third injections. The temperature is still low in these areas and the high temperature combustion has not been achieved yet. Later, the whole area occupied by the second and the third jets show increased formaldehyde production and finally we see the first spots of high temperature combustion occurring for the first time at the tip of the third jet. At the final stages of the process, the fuel concentrate in the near wall region

due to the first injection undergoes high temperature combustion as well. The same process takes place for every simulated case and it shows the importance of the injection strategy. For illustration reasons we show the evolution of ignition and combustion for OP4 in Fig. 27. The differences here are more pronounced and the succession of the processes is clearer.

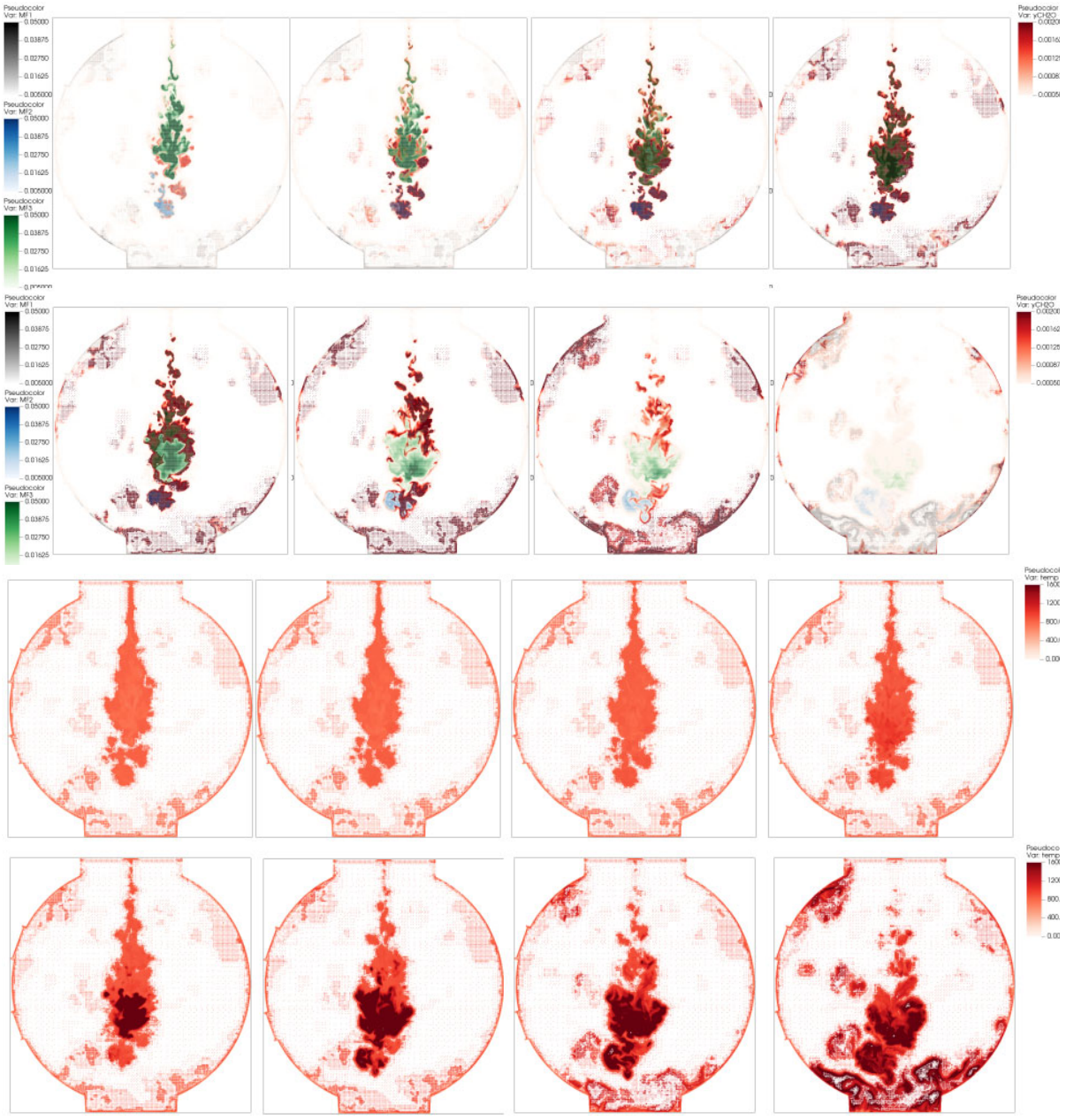

Fig. 26: Mixing, ignition and combustion for OP1. Upper rows: Mixture fraction corresponding to each of the three injections and formaldehyde mass fraction at certain timings after ignition. Lower rows: Temperature at the same time instants as the upper rows

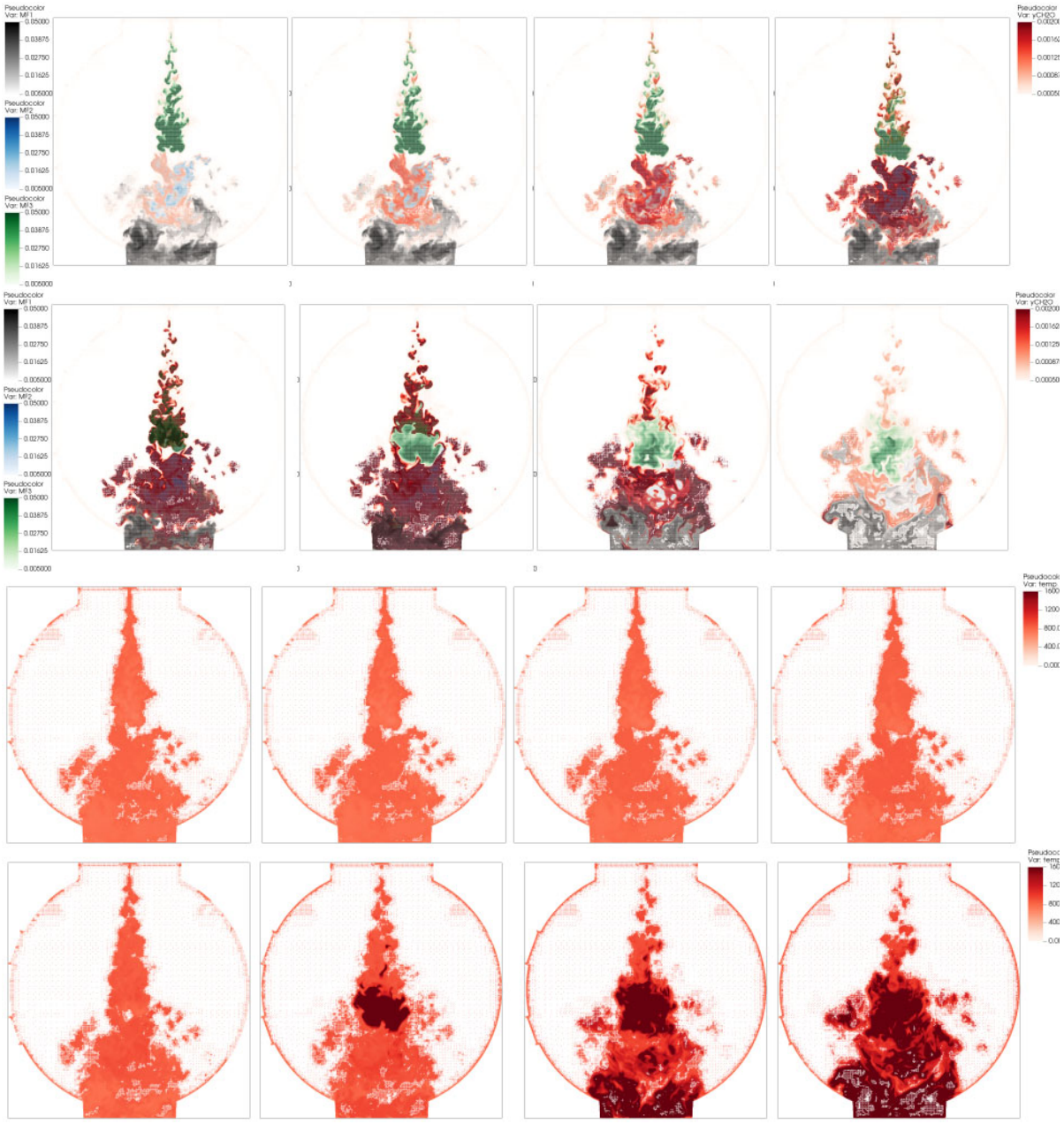

Fig. 27: Mixing, ignition and combustion for OP4. Upper rows: Mixture fraction corresponding to each of the three injections and formaldehyde mass fraction at certain timings after ignition. Lower rows: Temperature at the same time instants as the upper rows

4.5.1 Effect of chemistry mechanism employed

Our intention is to investigate the effect of different, in terms of complexity, chemistry schemes for h-heptane in the simulated dynamics of combustion. The skeletal mechanism of Liu et al. [49] consists of 44 species and 112 reactions. Its development is focused on high-pressure non-premixed autoignition conditions. A more detailed mechanism that was implemented and tested is the mechanism of Seiser et al. [50]. This mechanism consists of 159 species and 770 reactions. An even more detailed mechanism was implemented (Zhang et al. [51]), consisting of 1,268 species and 5,336 reactions, but

unfortunately its use proved to be unfeasible.The amount of time spent for temporal integration of the ODEs was orders of magnitude higher than the other mechanisms employed.

Both Liu and Seiser mechanisms agree well with experimental measurements for operating condition 1 with respect to HRR and integral HR (Fig. 28) in general. Both mechanisms predict ignition about 1 ms later than the experimentally measured value. Seiser mechanism predicts slightly earlier ignition and in order to elaborate on its ability to describe low temperature combustion the temporal evolution of formaldehyde (CH_2O) was investigated. As shown in Fig. 29, the earlier ignition predicted by the mechanism of Seiser et al. is not related to CH_2O production. Both mechanisms predict exactly the same start of formaldehyde production. Since the differences between the tested mechanisms proved to be minor, we chose to implement and conduct the rest of the simulations with the skeletal mechanism of Liu et al. [49] in order to reduce the computational cost.

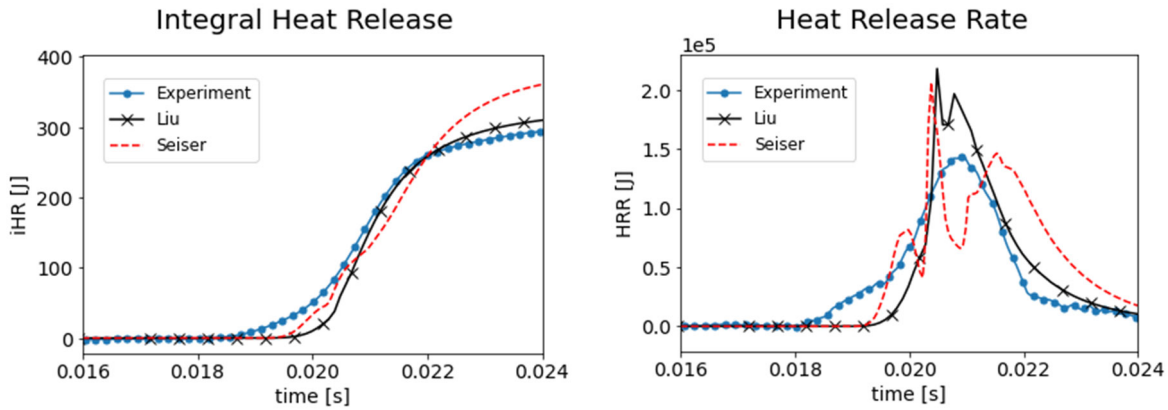

Fig. 28: Integral heat release (left) and heat release rate (right) as a function of time after the start of measurement for different chemistry mechanisms

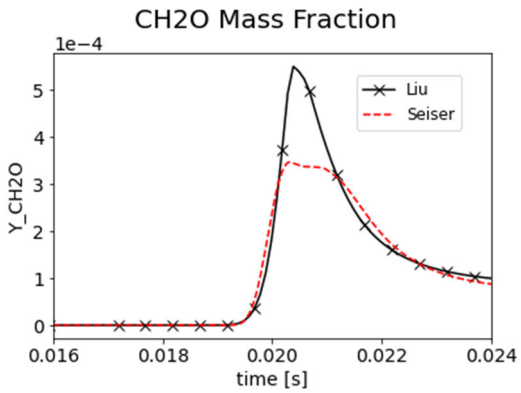

Fig. 29: Formaldehyde mass fraction as a function of time after the start of measurement for different chemistry mechanisms

4.5.2 Effect of film modelling

Due to the low-density environment experienced by the incoming jet, the penetration is expected to be higher. Hence a large part of the fuel impinges the wall and creates a thin liquid film. The importance of modeling this process is presented in Fig. 30: This plot shows iHR and HRR for operating condition 1 as a function of time after the start of measurement. When no film modeling is considered and it is assumed that all the fuel impinging on the wall rebounds in the domain, the total energy release is 25%

higher. Comparing this value with the experimentally measured iHR, then it is obvious that incorporating film modeling is necessary for reliable results.

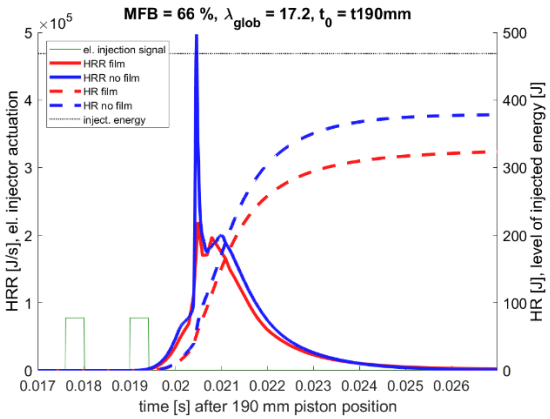

Fig. 30: iHR and HRR as a function of time after the start of measurement for the cases with and without film modeling

The numerical investigations in the RCEM are under review for FUEL.

4.6 Exploratory numerical simulation of engine relevant conditions

The final work package of this project targets in providing information about the mixing and ignition processes in multiple injection strategies employed in realistic engine conditions. The CFD methodology was employed successfully and validated thoroughly for the simulation of the processes in the RCEM. Due to the absence of experimental data at real engine conditions, the validated numerical methodology was applied to a hypothetical cylinder with similar geometric characteristics as the RCEM. The major change is the injection system: in the new setup, the injector, which consists of 8 adially distributed nozzles, is centrally located at the top of the cylinder. In order to investigate the mixing and film creation, two different umbrella angles are considered, namely 135 degrees and 80 degrees.

The combustion behaviour in the chamber is presented in Fig. 31 (left) for the two cases considered. It is observed that in both cases ignition occurs after the end of the third injection (vertical red line), illustrating the importance and educated choice of the injection strategy.

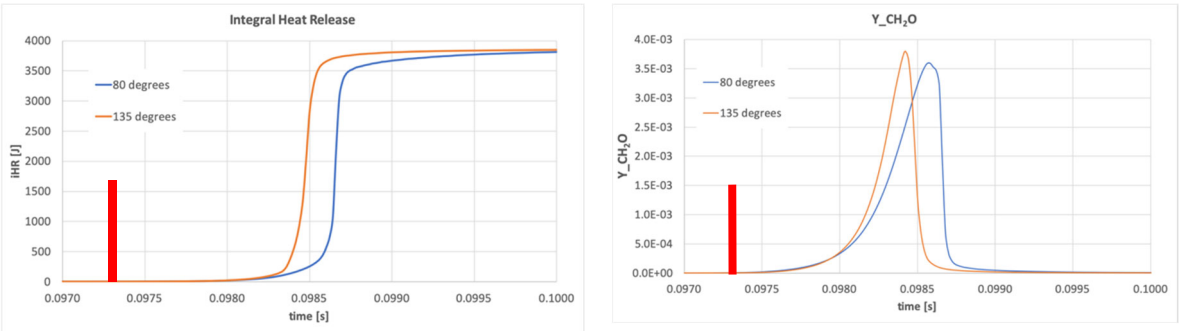

Fig. 31: iHR (left) and CH2O mass fraction (right) as a function of time for the cases with 80 and 135 degrees umbrella angle. The vertical red line designates the end of the 3rd injection.

Ignition occurs earlier in the case of the wide umbrella angle by roughly 2 ms. A more detailed picture of the ignition process can be obtained by following the evolution of the formaldehyde mass fraction shown in Fig. 31 (right).

After the end of the third injection, formaldehyde starts increasing in a similar manner in both cases, illustrating the presence of similar initial spots of suitable conditions in the area of the third injection. After this initial time interval, the differences in mixture stratification due to the different injection topologies results in enhanced formaldehyde production which is indicative of the presence of more spots under suitable conditions for ignition, leading to faster overall combustion.

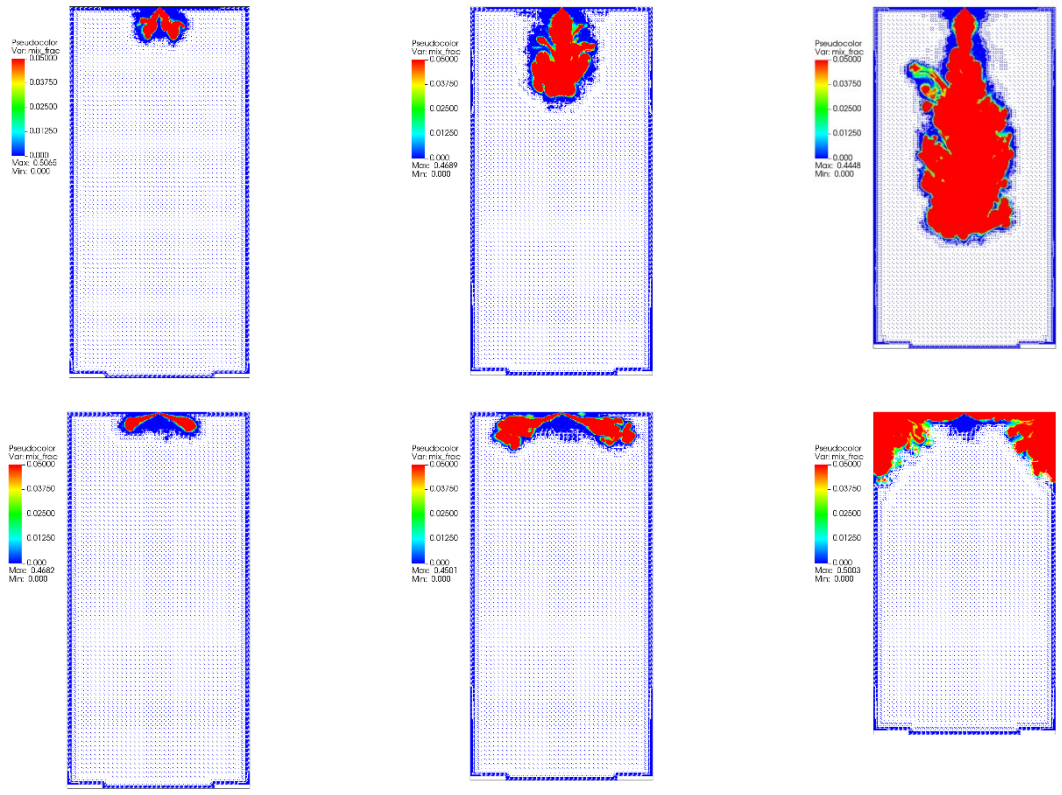

Fig. 32: Contour plot of mixture fraction for the 80 (upper row) and 135 (lower row) degrees umbrella angle cases during the first injection.

The mixing characteristics for each of the injection topologies are illustrated in Fig. 32: In the case with the small umbrella angle, the first spray penetrates deeper in the cylinder and during the interval until the latter injections, the mixture reaches a larger level of homogeneity with less significant stratification (Fig. 32, upper row). On the other hand, it is observed that the large umbrella angle results in high fuel concentration areas in the upper part of the cylinder and more specifically in the near wall regions. The stratification in this case is considerably more significant and pockets of increased fuel mixture fraction appear until late in the compression (Fig. 32, lower row). The earlier ignition and faster combustion occurring in the case of the large umbrella angle indicates that a certain level of mixture stratification is necessary. A characteristic of the large umbrella angle setup is the high deposition of fuel on the cylinder walls and the creation of a film. It has been already shown that detailed film modelling is necessary for resolving the complexities arising from the early injection in a low-density environment. Film creation intensifies stratification since the deposited fuel is evaporating later, during the low-volume high-temperature conditions close to the TDC. The mass deposited on the walls for the 135 degree umbrella angle case is three orders of magnitude larger compared to the 80 degree umbrella angle case Fig. 33. It is observed that before the second and third injections, most of the deposited fuel has already

evaporated. The vapour fuel remains in the vicinity of the wall leading to high local fuel concentrations in this area.

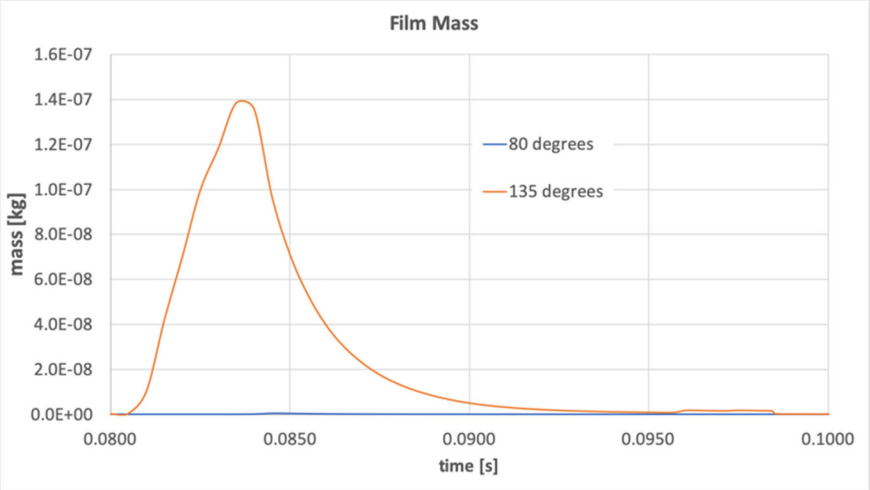

Fig. 33: Fuel mass deposited on the cylinder walls as a function of time for the cases with 80 and 135 degrees umbrella angle.

5 Conclusions

In this study, mixing, ignition and combustion behavior in an optically accessible RCEM operated under PCCI relevant conditions were investigated by combined passive optical and laser-optical high-speed diagnostics. The Schlieren technique was applied to extract fuel spray contours and jet metrics. In a reactive campaign, this was combined with CH_2O PLIF and OH^* chemiluminescence imaging to detect LT and HT ignition delay and location and to further characterize combustion. Corresponding equivalence ratio fields were obtained from tracer PLIF measurements under inert conditions. In order to achieve the balance between fuel-air mixture stratification and premixing that is required for the PCCI combustion mode, a split injection schedule consisting of a first long base load injection early in the compression stroke and two short injections close to TDC was used. The applied operating strategy resulted in only minor changes in engine metrics such as global equivalence ratio or compression ratio. Nevertheless, distinct differences in local fuel-air mixing and ignition behavior as well as combustion efficiency were observed. In focusing on the short double injection, the analysis of the optical data revealed several key findings:

1. Previous experimental and numerical studies of closely coupled double injections under constant ambient conditions showed an increased penetration rate of the subsequent fuel spray caused by the persistent momentum of the preceding jet [19, 22, 30]. Under transient RCEM conditions, however, the aerodynamic gain from the preceding injection is counteracted by the density rise during the compression stroke, eventually leading to shorter penetrations of the consecutive jet.
2. In a double injection scheme, mixing of the subsequent fuel spray benefits from the turbulence induced by the preceding jet [19, 21, 22]. Although the shorter penetration of the subsequent jet during RCEM operation is confirmed by the equivalence distribution, an enhanced mixing rate of the second fuel spray is found for all investigated conditions. It is shown that, in contrast to the typical stagnation plane structure at the head of the preceding spray, the consecutive jet exhibits a significantly smoother gradient of the equivalence ratio at the spray tip, indicating faster mixing [22]. This is further quantified for all OPs by comparing the integrated cross-sectional average equivalence ratio at the spray head and tail of preceding and subsequent injection, revealing

consistently faster mixing for the consecutive jet with an almost constant offset in the tail region, but substantial differences at the spray head.

3. The analysis of the mixing state within the laser light sheet after the first base load injection exhibits substantial differences resulting from the operating strategy. Although these marked differences in premixing are observed, all OPs approach a similar mixing state at the end of the following double injection event. Therefore, it is concluded that the in-plane mixing state is not determined by the operating strategy but dominated by the double injection event, the latter being identical for all OPs.

4. Even though variations in operating parameters are small, the thermodynamic analysis reveals a distinctly different combustion behavior between the OPs. All HRR curves display a gradual increase associated with the LT fuel oxidation, followed by a steep rise as a consequence of HT combustion. Since the mass fraction burned is significantly below 100 % in all OPs, three out of four HRR curves display post-combustion heat release by a persistent LT reactivity. From a further analysis of ignition timings it is found that more than 20 % of the overall heat release can be attributed to LT oxidation reactions before the actual onset of HT combustion.

5. The analysis of LT ignition characteristics reflects the complex interplay between mixing dynamics and reaction kinetics. The onset of LT reactivity after the 2nd injection is found to be dominated by the operating strategy and the resulting variation in bulk temperature. Regarding the location of LT ignition, however, a distinct relationship to the local mixing state is revealed: Whereas the entrainment of fuel mass from the 1st injection by the 2nd jet leads to richer upstream mixtures and thus favors the onset of LT oxidation reactions, the absence of base load fuel in the near nozzle area results in fast leaning of the spray tail, so that LT ignition is shifted towards the richer spray head. An immediate onset of LT reactivity is observed when the 3rd fuel spray expands into hot LT combustion products from the preceding 2nd jet [19, 22]. In the absence of prevailing LT oxidation reactions, LT reactivity of the 3rd jet is triggered by suitable ambient conditions. In addition, aerodynamic effects induced by the sustained momentum of the 2nd jet promote the transition of the mixing field at the spray head of the 3rd injection from a stagnation plane structure to a smoothly decaying equivalence ratio distribution and, thereby, further accelerate the onset of LT reactivity.

6. The HT ignition process is observed to be significantly influenced by the local mixing state in combination with the interaction between aerodynamics and combustion chemistry. Two distinct HT ignition events are identified for OPs 1, 2 and 4, which are associated with the arrival of the 2nd and the 3rd fuel spray, respectively. When comparing the two ignition events, the first occurs at much leaner conditions with ignition delays twice as long and at a notably larger axial distance from the injector nozzle. Regarding the second ignition event, it is shown that, even though similar ambient conditions prevail, the absence of LT combustion products in the upstream region leads to a prolonged HT ignition delay. In contrast, the entrainment of persistent upstream LT reactivity by the subsequent fuel spray results in shorter HT ignition delays and smaller axial distances of the initial reaction zone from the injector.

7. A sustained CH_2O PLIF signal is observed in all OPs after HT combustion has finished, which is related to post-combustion LT oxidation reactions of the unburned fuel mass [19]. Compared to low signal levels prior to HT combustion, post-combustion fluorescence intensities are much higher, which, however, do not reflect the contribution of post-combustion LT reactivity to the overall heat release. It is argued, that even though the high temperature and pressure environment after HT combustion should promote quenching of formaldehyde fluorescence, this is overcompensated by the low oxygen content of the burnt gas. However, the quenching rate of formaldehyde fluorescence by oxygen under high temperature and pressure conditions has to be considered largely unknown, so that investigations in that direction would be highly desirable.

Above findings provide a conclusive analysis of mixing, ignition and combustion characteristics related to PCCI operation using a split injection schedule under transient engine conditions. In summary, the study provides clear evidence that even small changes in the operating strategy have significant

influence on the local mixing state and reaction kinetics, which ultimately develop a huge impact on the overall engine efficiency.

A validated detailed numerical methodology based on LES is developed and used for the simulation of the mixing and combustion processes in the RCEM. The developed methodology is versatile and accurate. Different models were tested and the sensitivity of the results with respect to different modeling approaches was investigated. In addition, several chemistry mechanisms were employed. It is found that none of the tested mechanisms can accurately capture the formaldehyde production in the low combustion regime, although CH_2O in all of them acts as a precursor to high temperature combustion. Implementation of film modeling is of paramount importance due to the presence of an early injection in a low-density environment. The global thermodynamic properties as well as global mixing were extracted and compared with experimental measurements. The numerical results showed very good quantitative agreement with the measurements for most of the simulated cases. Detailed analysis of the mixing and ignition illustrated a certain pattern, which is consistent with the experimentally observed phenomena. Finally, engine relevant conditions were considered and the influence of the spray topology was investigated. It was shown that the injection strategy tested on the RCEM works as expected also at engine relevant conditions.

Overall, considerable scientific progress is reported for partially Premixed Compression Ignition Combustion at engine relevant conditions employing multiple injections to tailor the level of stratification, by combining optical diagnostics and Large-Eddy Simulations with detailed chemical kinetics. In terms of practical application, a number of open questions remain: I) quantitative emissions measurements from PCCI engine operation are required, as these are difficult to quantify in single-shot configurations such as the employed Rapid Compression Expansion Machine. II.) more work is needed to develop suitable injection schedules towards reducing spray/wall interaction and improve overall fuel conversion and III) the findings point towards novel/synthetic fuels with improved evaporation and mixing characteristics and good ignition propensity as promising candidates to address such problems. Future studies in the field of lowest-emission compression ignition combustion are therefore clearly warranted. as such combustion modes – in combination with renewable energy carriers – are projected to dominate heavy-duty freight transport, on/off-road machinery as well as the shipping sector for several decades to come.

6 Outlook and next steps

While key phenomena have been identified in terms of interplay between chemistry and turbulence in the context of multiple injections, early injections to prepare a largely premixed substrate were found to show considerable wall impingement due to the low back pressure. As a consequence, the overall fuel conversion was found to be rather low. Further investigations to identify appropriate injection schedules are required for optimal performance. In addition, the single-shot nature of the RCEM precluded NOx and soot measurements to assess the performance of the studied configurations in terms of emissions. Engine experiments – originally foreseen in parallel – are a prerequisite for further advances in the field. Nonetheless, the combined experimental and numerical efforts provide a solid fundamental background for future efforts and the knowhow gained will be indispensable to interpret future engine measurements and relations between thermodynamic and emission data as a function of operating strategy.

In addition, PCCI appears a particularly attractive concept also for lower boiling point fuels with high ignition propensities, which could be synthesized from renewable sources/e-fuels. In particular DME constitutes an interesting candidate, since it is injected at supercritical conditions, exhibiting good mixture formation and potentially avoiding significant wall impingement. Furthermore, due to the absence of any C-C bonds, low sooting propensity has been demonstrated for conventional Diesel combustion. This suggests that DME could be an ideal candidate to achieve lowest-emission energy conversion employing different combustion modes for specific engine load points and should therefore be further investigated in future studies.

7 National and international cooperation

This project is co-funded by the FVV Project “Premixed Diesel/PCCI” and carried out in collaboration with the institute of vehicle systems (IFS) of Stuttgart University.

The experiments at the RCEM were performed by Dr. Ulrich Doll, PSI, MSc. M. Todino and Dr. Christophe Barro LAV/ETHZ. A considerable share of the simulation activities were carried out by Ms. María Martínez García, a visiting PhD candidate from CMT Motores Térmicos, Universitat Politècnico de València, Spain in close collaboration with Dr. Altantzis, LAV/ETHZ.

Fruitful discussions in the context of multiple injections in the spray task of the Technical Collaboration Programme “Clean and efficient combustion” of the International Energy Agency are also gratefully acknowledged.

8 Publications

The experimental study was successfully published in FUEL, while the numerical investigations in the RCEM were also submitted to FUEL and are still under review.

All work carried out at LAV, ETH Zurich was presented at the FVV Spring Conference 2021 and the corresponding conference report. The final report to FVV is still awaiting inclusion of the engine related investigations at Stuttgart University.

9 References

1. Srna, A., et al., *Effect of methane on pilot-fuel auto-ignition in dual-fuel engines.* Proceedings of the Combustion Institute, 2019. **37**(4): p. 4741-4749.
2. Kammermann, T., et al., *Generation of Turbulence in a RCEM towards Engine Relevant Conditions for Premixed Combustion Based on CFD and PIV Investigations.* Sae International Journal of Engines, 2017. **10**(4): p. 2176-2190.
3. Srna, A., et al., *Experimental investigation of pilot-fuel combustion in dual-fuel engines, Part 1: Thermodynamic analysis of combustion phenomena.* Fuel, 2019. **255**.
4. Schlatter, S., et al., *Experimental Study of Ignition and Combustion Characteristics of a Diesel Pilot Spray in a Lean Premixed Methane/Air Charge using a Rapid Compression Expansion Machine*, in *SAE World Congress & Exhibition*. 2012, SAE International.
5. Mitakos, D.A., et al., *Integration of a Cool-Flame Heat Release Rate Model into a 3-Stage Ignition Model for HCCI Applications and Different Fuels*, in *SAE World Congress & Exhibition*. 2014, SAE International.
6. Obrecht, P., *WEG - Wärmeentwicklungsgesetz, Rechenprogramm zur thermodynamischen Analyse aus Brennraumdruckverläufen*. 2007, ETH Zürich/LAV.
7. Mitakos, D., et al., *Ignition Delays of Different Homogeneous Fuel-air Mixtures in a Rapid Compression Expansion Machine and Comparison with a 3-Stage-ignition Model Parameterized on Shock Tube Data*, in *SAE/KSAE International Powertrains, Fuels & Lubricants Meeting*. 2013, SAE International.
8. Srna, A., et al., *Experimental investigation of pilot-fuel combustion in dual-fuel engines, Part 2: Understanding the underlying mechanisms by means of optical diagnostics.* Fuel, 2019. **255**.
9. Pickett, L.M. *Engine Combustion Network*. 2013 [cited 2020; Available from: https://ecn.sandia.gov/.
10. Srna, A., *Experimental Characterization of Pilot-Fuel Ignition, Combustion, and Soot Formation in Dual-Fuel Combustion Systems*. 2018, ETH Zurich.

11. Bruneaux, G., *Mixing Process in High Pressure Diesel Jets by Normalized Laser Induced Exciplex Fluorescence Part I: Free Jet*, in *SAE Brasil Fuels & Lubricants Meeting*. 2005, SAE International.
12. Sakellarakis, V.D., et al., *The effect of high-pressure injection variations on the mixing state of underexpanded methane jets.* International Journal of Engine Research, 2020. **OnlineFirst**.
13. Yeh, C.-N., et al., *Quantitative Measurement of 2-D Fuel Vapor Concentration in a Transient Spray via Laser-Induced Fluorescence Technique*, in *SAE International Fuels & Lubricants Meeting & Exposition*. 1994, SAE International.
14. Senda, J., et al., *Quantitative Analysis of Fuel Vapor Concentration in Diesel Spray by Exciplex Fluorescence Method*, in *SAE International Congress & Exposition*. 1997, SAE International.
15. Kim, T., et al., *Evaporating Spray Concentration Measurementsfrom Small and Medium Bore Diesel Injectors*, in *SAE World Congress & Exhibition*. 2002, SAE International.
16. Dent, J.C., *A Basis for the Comparison of Various Experimental Methods for Studying Spray Penetration*, in *SAE International Mid-Year Meeting* 1971, SAE International.
17. Hiroyasu, H. and M. Arai, *Fuel Spray Penetration and Spray Angle in Diesel Combustion Chamber* in *Transactions SAE of Japan*. 1980, SAE International. p. 5-11.
18. Naber, J.D. and D.L. Siebers, *Effects of Gas Density and Vaporization on Penetration and Dispersion of Diesel Sprays*, in *SAE International Congress & Exposition* 1996, SAE International.
19. Skeen, S., J. Manin, and L.M. Pickett, *Visualization of Ignition Processes in High-Pressure Sprays with Multiple Injections of n-Dodecane.* Sae International Journal of Engines, 2015. **8**(2): p. 696-715.
20. Musculus, M.P.B. and K. Kattke, *Entrainment Waves in Diesel Jets.* SAE Int. J. Engines, 2009. **2**(1): p. 1170-1193.
21. Zhang, Y., T. Ito, and K. Nishida, *Characterization of Mixture Formation in Split-Injection Diesel Sprays via Laser Absorption-Scattering (LAS) Technique*, in *SAE International Fall Fuels & Lubricants Meeting & Exhibition* 2001, SAE International.
22. Bruneaux, G. and D. Maligne, *Study of the Mixing and Combustion Processes of Consecutive Short Double Diesel Injections.* SAE International Journal of Engines, 2009. **2**(1): p. 1151-1169.
23. Dahms, R.N., et al., *Understanding the ignition mechanism of high-pressure spray flames.* Proceedings of the Combustion Institute, 2017. **36**(2): p. 2615-2623.
24. Barro, C., et al., *Development and Experimental Validation of a Fast Spray Ignition Model for Diesel Engines Using Insights from CFD Spray Calculations.* SAE International Journal of Fuels and Lubricants, 2017. **10**(2): p. 304-317.
25. Barro, C., et al., *Investigation of the Ignition Process of Pilot Injections Using CFD*, in *14th International Conference on Engines & Vehicles*. 2019, SAE International.
26. Metz, T., et al., *Fluorescence lifetimes of formaldehyde (H2CO) in the Ã1A2→X̃1A1 band system at elevated temperatures and pressures.* Spectrochimica Acta Part A: Molecular and Biomolecular Spectroscopy, 2004. **60**(5): p. 1043-1053.
27. Yamasaki, Y. and A. Tezaki, *Non-linear pressure dependence of A-state fluorescence lifetime of formaldehyde.* Applied Physics B, 2005. **80**(7): p. 791-795.
28. Desantes, J.M., et al., *Optical study on characteristics of non-reacting and reacting diesel spray with different strategies of split injection.* International Journal of Engine Research, 2019. **20**(6): p. 606-623.
29. Doll, U., et al., *Impact of a split injection strategy on mixing, ignition and combustion behavior in Premixed charge compression ignition combustion.* Fuel, 2021. **294**.
30. Hadadpour, A., M. Jangi, and X.S. Bai, *Jet-jet interaction in multiple injections: A large-eddy simulation study.* Fuel, 2018. **234**: p. 286-295.